Computers & Fluids 116 (2015) 205–228

Contents lists available at ScienceDirect

Computers & Fluids

journal homepage: www.elsevier.com/locate/compfluid

A Smoothed Particle Hydrodynamics model for 3D solid body transport in free surface flows

Andrea Amicarelli [a,*], Raffaele Albano [b], Domenica Mirauda [b], Giordano Agate [a], Aurelia Sole [b], Roberto Guandalini [a]

[a] Ricerca sul Sistema Energetico – RSE SpA, Department SFE (formerly ASV), Italy
[b] Basilicata University, School of Engineering, Italy

ARTICLE INFO

Article history:
Received 28 July 2014
Received in revised form 17 April 2015
Accepted 25 April 2015
Available online 5 May 2015

Keywords:
SPH
Mesh-less
Particle methods
Dam break
Floating bodies
Floods

ABSTRACT

This study has developed a 3D Smoothed Particle Hydrodynamics (SPH) numerical scheme to reproduce the transport of rigid bodies in free surface flows (e.g. floods, surface waves). It is based on the Euler–Newton equations for body dynamics, implemented through the SPH formalism. This scheme has been coupled to a Weakly Compressible (WC)-SPH model for the main flow, based on the semi-analytic approach (Di Monaco et al. 2011). The SPH boundary treatment of Adami et al. (2012) has been implemented and adapted to free-slip conditions to model the "fluid–solid body" coupling terms. On the other hand, the "solid–solid" ("body–body" and "body–frontier") interactions are represented by the "boundary force particles" of Monaghan (2005). This technique has been implemented by introducing some modifications to represent the impingements of entire bodies (not only isolated particles), even at low velocities.

The new model has been validated on a sequence of 2D and 3D test cases. They involve preliminary tests both with single and multiple bodies and frontiers, four water entries of falling solid wedges, and the propagation of a 3D dam break front. This is driven by the regular lift of a mobile gate, transports a floating body (6 degrees of freedom) and impacts two fixed obstacles and several solid frontiers. This last phenomenon has also been experimentally realized during this study. Validation refers to comparisons vs. measurements, Unsteady Reynolds-Averaged Navier–Stokes (URANS) results, other SPH models, analytical and theoretical solutions.

1. Introduction

Smoothed Particle Hydrodynamics represents a mesh-less Computational Fluid Dynamics (CFD) technique for free-surface and multi-phase flow modelling [1–3]. A main advantage of this method concerns a direct estimation of the position of free surface, inter-fluid, inter-phase, and fluid–solid interfaces. At the same time, SPH modelling involves the computation of Lagrangian derivatives on the Left Hand Sides (LHS) of the fluid dynamics balance equations, where there is no need to explicitly treat the convective non-linear terms. Furthermore, no computational mesh is involved and the numerical algorithms are quite simple. So far, SPH modelling has been explored on several hydraulics application fields such as floods (e.g. [4,5]), coastal (e.g. [6]) and maritime (e.g. [7–9]) engineering, fluid–structure interactions (e.g. [10–12]), biomedical engineering, sloshing phenomena (e.g. [13–15]), landslide modelling (e.g. [16]), turbomachines (e.g. [17,18]), accidents (e.g. fluid leakages, [20]), bubble dynamics (e.g. [21]), magneto-hydrodynamics and astrophysical applications (e.g. [22–25]),...

Besides, SPH technique can simultaneously deal with multiple body dynamics, as usually developed in astrophysics and solid mechanics. However, only few SPH models have been conceived to represent the transport of moving bodies, driven by free surface flows. The main difficulties arise from the treatment of each of the multiple 2-way fluid–body and solid–solid (body–body and body-boundary) interactions. Several application fields could benefit from this modelling, such as floods (river overflows or dam breaks) and industrial accidents triggered by natural events (Na-Tech, [26]), with fluid flows transporting solid structures, vehicles, tree trunks, ice floes..., or the motion of floating bodies driven by gravitational surface waves (e.g. floating platforms, buoys, off-shore and on-shore foundations and structures). In this last case, the standard approaches often fail as linear and

* Corresponding author.
E-mail addresses: Andrea.Amicarelli@rse-web.it (A. Amicarelli), albano.raffaele@tiscali.it (R. Albano), domenica.mirauda@unibas.it (D. Mirauda), Giordano.Agate@rse-web.it (G. Agate), aurelia.sole@unibas.it (A. Sole), Roberto.Guandalini@rse-web.it (R. Guandalini).

http://dx.doi.org/10.1016/j.compfluid.2015.04.018
0045-7930/

second-order wave diffraction theory does not represent highly non-linear effects associated with extreme waves.

In the following of this introduction, we briefly recall the basis of the SPH approach, with a particular focus on boundary treatment, and then describe the state-of-the-art of this technique in modelling rigid solid bodies driven by free surface or confined flows.

Smoothed Particle Hydrodynamics represents a particle method (each particle is considered as a computational node), based on an interpolative approach.

Let us first consider the representation of a generic function f (at a generic computational point $\underline{x}_0$) as the convolution integral (over the infinite space) of the same f, weighted by the Dirac's delta (δ_D):

$$f(\underline{x}_0) = \int_{V_\infty} f(\underline{x})\delta_D(\underline{x} - \underline{x}_0)dx^3 \tag{1.1}$$

Hereafter, the under-bar symbol denotes a vector. SPH approximates (1.1) to represent the functions and derivatives appearing in the balance equations of fluid dynamics. In fact, SPH considers convolution integrals over a limited space, the kernel support V_h (a sphere of radius 2 h, h being the kernel support size). The computational point is represented by the co-moving particle position. SPH then uses an analytical smoothing/weighting function (or kernel: W or $W(\underline{x} - \underline{x}_0)$), [27]), which replaces the Dirac's delta.

In particular, the SPH approximation in the continuum (integral SPH approximation $\langle\rangle_I$) of a generic function ($f(x)$ or f) is defined as:

$$\langle f\rangle_{I\underline{x}_0} = \int_{V_h} f(\underline{x})W(\underline{x} - \underline{x}_0, h)dx^3 \tag{1.2}$$

Applying the same operator to a generic derivative, computed along the spatial component x_i, the integral SPH approximation provides the following equation (after integration by parts):

$$\left\langle \frac{\partial f}{\partial x_i}\middle| \right\rangle_{I\underline{x}_0} = \int_{V_h} W\frac{\partial f}{\partial x_i}dx^3 = \int_{A_h} Wfn_i dx^2 - \int_{V_h} f\frac{\partial W}{\partial x_i}dx^3 \tag{1.3}$$

Here $\underline{n}$ is the unity vector locally normal to the boundary.

The discretization of the volume integral in the last term of (1.3) will consider fluid particles (called "neighbouring/neighbour particles") around the computational particle (Section 2). On the other hand, the surface integral in (1.3) should be computed over the boundary (A_h) of the kernel support. The representation of this term is a key point in SPH boundary treatment, for several reasons. First, the SPH truncation error at boundaries is relevant if we strictly integrate the surface term in (1.3). Further, imposing boundary conditions on a surface frontier is not trivial, when starting from a Lagrangian field of non-uniformly distributed moving particles. Modelling this boundary term is then crucial, as both (1.2) and (1.3) may be affected by truncation errors at the frontiers of the fluid domain [28,29], if they are modelled straightforwardly. In this context, several numerical methods have been proposed and validated. Some of them are briefly discussed below.

Monaghan [1] and Monaghan and Kajtar [30] define repulsive forces at the fluid–boundary interface, called "boundary force particles". Other techniques adopt the so-called "ghost" [5,1] or "mirror" [31] particles, as fictitious neighbouring particles, which lie outside the fluid domain and complete the truncated kernel supports at boundaries. A similar technique has been recently developed by Adami et al. [32], who impose correct boundary no-slip conditions, even for accelerated fluid–solid interfaces. Di Monaco et al. [33] numerically developed the semi-analytic approach, as originally formulated by Vila [34]: this represents a sort of integral version of the mirror particles of Adami et al. [32], for fixed boundaries. On the other hand, Ferrand et al. [35], Mayrhofer et al. [36], and Ferrari et al. [39] use similar boundary treatments, which rely on a direct modelling of the surface boundary integrals at the frontiers of the fluid domain, according to a complete and corrected SPH approximation of a derivative (1.3). Finally, other advanced models (e.g. [17,19]) use the Arbitrary Lagrangian–Eulerian formalism to write the balance equations of fluid dynamics, whose weak formulation directly treats boundaries (SPH-ALE approach) and adopts upwind schemes to improve the SPH spatial accuracy. These schemes have been also implemented in fully Lagrangian SPH models (strong formulation of balance equations), especially to correct the continuity equation (e.g. [37,38]) or estimate pressure at boundaries [39].

At the same time, only few SPH studies have dealt with the transport of solid bodies driven by free surface or confined flows. They mainly refer to 2D and single interface interactions. They are briefly described in the following.

Oger et al. [40] use the ghost particle method to model a 2D dynamics of a falling wedge into still water. Monaghan et al. [41] represent the interactions between water surface waves and fixed cylinders through the use of the boundary force particles. Using the same technique, Omidvar et al. [42,43] model the fluid–body interaction terms to represent a floating body, driven by surface waves (in 2D and 3D respectively). Adopting the same type of particles, Kajtar and Monaghan [44] reproduces 2D modular bodies in confined flows and Valizadeh and Monaghan [45] also simulate rigid mobile frontiers and their interactions with fluid flows. The boundary force particles are still applied by Kajtar and Monaghan [46], where the authors also use repulsive forces to model solid–boundary interactions. Hashemi et al. [47] represent the transport of 2D bodies in confined visco-elastic flows, deriving a formulation similar to Adami et al. [32] for fluid–solid interactions, but introducing modifications to increase accuracy and deal with shear stresses. They also use repulsive forces, defined for body–body impingements. The same authors represent the transport of 2D bodies in confined flows in Hashemi et al. [48]. Anghileri et al. [49] model the 3D impact of a falling parallelepiped on still water coupling a Finite Element Method code (solid modelling) with an SPH model for the fluid domain. Finally, Seungtaik et al. [50] directly represent solid–solid interactions applying the equation which describes the collision of two rigid bodies in 3D (approximated using a SPH formalism) and providing qualitative validations.

In this context, we have developed and validated a 3D SPH scheme for body transport in free surface flows. We have coupled it to an SPH model for the main flow, based on the semi-analytic approach [33]. The formulation of the fluid–body interaction terms is based on an adaptation of the boundary technique of Adami et al. [32], whose original formulation was quantitatively validated on fixed frontiers (2D). Here we implement and apply a variant of it, in order to model free-slip conditions. Body–body and body–boundary impingements are represented according to the boundary force particles, as formulated by Monaghan [1], here implemented and adapted to treat whole solid bodies (not only particle impingements), even at low velocities.

The resulting RSE model has been validated using 2D and 3D reference test cases, where measures, analytical solutions, theoretical methods, other SPH and Unsteady Reynolds-Averaged Navier–Stokes (URANS) numerical results are available. In particular the main test case, a dam break event with 3D body transport, has also been experimentally realized during this study, at Basilicata University.

After this introduction (Section 1), Section 2 describes the numerical model, Section 3 the sequence of validation tests and Section 4 the overall conclusions.

2. The numerical model

This section describes the main features of the numerical model here presented, by analysing the balance equations for fluid (Section 2.2) and body (Section 2.3) dynamics and then the

2-way interaction terms related to both fluid–body (Section 2.3) and solid–solid (Section 2.4) interactions.

2.1. SPH approximation of the balance equations of fluid dynamics

The numerical scheme for the main flow refers to a Weakly-Compressible (WC) SPH model and the semi-analytic approach for boundary treatment. Its basic features are deeply described in Di Monaco et al. [33] and here briefly reported.

Let refer to Euler's momentum and continuity equations, in the following forms:

$$\frac{du_i}{dt} = -\frac{1}{\rho}\frac{\partial p}{\partial x_i} - \delta_{i3}g = -\frac{\partial (p/\rho)}{\partial x_i} - \frac{p}{\rho^2}\frac{\partial \rho}{\partial x_i} - \delta_{i3}g, \quad i = 1,2,3$$
$$\frac{d\rho}{dt} = -\rho \nabla \cdot \underline{u} \tag{2.1}$$

where $\underline{u} \equiv (u, v, w)$ is the velocity vector, p pressure, ρ the fluid density, δ_{ij} Kronecker's delta, $\underline{x}$ position and t time. We need to compute them at each fluid particle position using the SPH formalism and take into account the boundary terms (fluid–frontier and fluid–body interactions), as described in the following.

Let consider an SPH approximation of (2.1). For this purpose, we refer to the SPH representation of a generic derivative (1.3) according to the semi-analytic approach ("$_{SA}$"; [34]):

$$\left\langle \frac{\partial f}{\partial x_i} \right\rangle_{SA,0} = \sum_b (f_b - f_0)\frac{\partial W_b}{\partial x_i}\omega_b + \int_{V_h'} (f - f_0)\frac{\partial W}{\partial x_i} dx^3 \tag{2.2}$$

This formula represents an approximation of the first equality in (1.3). The inner fluid domain here involved is filled with numerical particles to represent the summation in (2.2). At boundaries, we formally do not truncate the kernel support and the kernel sphere can partially lie outside the fluid domain. In other words, the summation in (2.2) is performed over all the fluid particles "$_b$" (neighbouring particles with volume ω) in the kernel support of the computational fluid particle ("$_0$"). At the same time, the volume integral in (2.2) represents the boundary term, which is a convolution integral on the truncated portion of the kernel support. In this fictitious and outer volume (V_h'), we need to define the generic function f (pressure, velocity or density alternatively).

The semi-analytic approach ("$_{SA}$"), as interpreted by Di Monaco et al. [33], hypothesizes the following linearization and assumptions to compute f in V_h':

$$f \cong f_{SA} + \left.\frac{\partial f}{\partial x_i}\right|_{SA}(\underline{x} - \underline{x}_0) \Rightarrow \left\langle \frac{\partial f}{\partial x_i} \right\rangle_{SA} = \sum_b (f_b - f_0)\frac{\partial W_b}{\partial x_i}\omega_b + \int_{V_h'} f_{SA}\frac{\partial W}{\partial x_i} dx^3 + \int_{V_h'} \left.\frac{\partial f}{\partial x_i}\right|_{SA}(\underline{x} - \underline{x}_0)\frac{\partial W}{\partial x_i} dx^3 \tag{2.3}$$

The peculiar "$_{SA}$" values of the functions and derivatives in V_h' are assigned to represent a null normal gradient of reduced pressure at a frontier interface (considering uniform density):

$$p_{SA} = p_0, \quad \left\langle \frac{\partial p}{\partial x_i} \right\rangle_{SA} = -\delta_{i3}g; \quad \rho_{SA} = \rho_0, \quad \left\langle \frac{\partial \rho}{\partial x_i} \right\rangle_{SA} = 0 \tag{2.4}$$

At the same time, we approximately set free-slip conditions when estimating velocity at boundaries. The velocity vector is taken as uniform in the outer part of the kernel support. Here $\underline{u}_{SA}$ is decomposed in the sum of a vector normal to boundary ($\underline{u}_{SA,n}$) and a tangential vector ($\underline{u}_{SA,T}$). The first is represented as a linear extrapolation from the computational fluid particle velocity. The latter is equal to its analogous vector of the same fluid particle (the subscript "$_w$" refers to a generic frontier):

$$\left.\begin{array}{l} \underline{u}_{SA} = \underline{u}_{SA,T} + \underline{u}_{SA,n} \equiv u_{0,T} + [(2\underline{u}_w - \underline{u}_0)\cdot \underline{n}]\underline{n} \\ \underline{u}_{SA,T} \equiv \underline{u}_{0,T}, \quad \left\langle \frac{\partial u_i}{\partial x_i} \right\rangle_{SA} = 0 \end{array}\right\} \Rightarrow \underline{u} - \underline{u}_0 = \underline{u}_{SA} - \underline{u}_0 = 2[(\underline{u}_w - \underline{u}_0)\cdot \underline{n}]\underline{n} \tag{2.5}$$

We can now write the continuity equation for a Weakly Compressible SPH model (Einstein's notation works for "$_j$"), using the semi-analytic approach as a boundary treatment:

$$\left\langle \frac{d\rho}{dt} \right\rangle_0 = \sum_b \rho_b (u_{b,j} - u_{0,j})\left.\frac{\partial W}{\partial x_j}\right|_b \omega_b + 2\rho_0 \int_{V_h'} [(\underline{u}_w - \underline{u}_0)\cdot \underline{n}]n_j \frac{\partial W}{\partial x_j} dx^3 + \underline{C}_s \tag{2.6}$$

where $\underline{C}_s$ is introduced to represent a fluid–body interaction term, as presented in Section 2.3.

On the other hand, we can analogously derive the approximation of the momentum equation (the notation $\langle\rangle$ indicates the SPH particle – discrete – approximation):

$$\begin{aligned} \left\langle \frac{du_i}{dt} \right\rangle_0 = {} & -\delta_{i3}g + \sum_b \left(\frac{p_b}{\rho_b^2} + \frac{p_0}{\rho_0^2}\right)\left.\frac{\partial W}{\partial x_i}\right|_b m_b + 2\frac{p_0}{\rho_0}\int_{V_h'} \frac{\partial W}{\partial x_i} dx^3 \\ & - \upsilon_M \sum_b \frac{m_b}{\rho_0 r_{0b}^2}(\underline{u}_b - \underline{u}_0)\cdot(\underline{x}_b - \underline{x}_0)\left.\frac{\partial W}{\partial x_i}\right|_b \\ & - 2\upsilon_M(\underline{u}_w - \underline{u}_0)\cdot \int_{V_h'} \frac{1}{r_{0w}^2}(\underline{x} - \underline{x}_0)\frac{\partial W}{\partial x_i} dx^3 + \underline{a}_s \end{aligned} \tag{2.7}$$

where $\underline{a}_s$ represents a new acceleration term due to the fluid–body interactions (Section 2.3), υ_M is the artificial viscosity [1], m the particle mass and $\underline{r}$ the relative distance between the neighbouring and the computational particle.

Time integration is performed according to a second-order Leapfrog scheme (let refer to Violeau and Leroy [51] for stability analysis and time integration schemes in SPH modelling):

$$\begin{aligned} & x_{i,0}|_{t+dt} = x_{i,0}|_t + u_{i,0}|_{t+dt/2}\, dt, \quad i = 1,2,3 \\ & u_{i,0}|_{t+dt/2} = u_{i,0}|_{t-dt/2} + \left\langle \frac{du_{i,0}}{dt} \right\rangle\Big|_t dt, \quad i = 1,2,3 \\ & \rho_0|_{t+dt} = \rho_0|_t + \left\langle \frac{d\rho_0}{dt} \right\rangle\Big|_{t+dt/2} dt \end{aligned} \tag{2.8}$$

Finally a barotropic equation of state is linearized as follows:

$$p \cong c_{ref}^2\left(\rho - \rho_{ref}\right) \tag{2.9}$$

The artificial sound speed c is 10 times higher than the maximum fluid velocity (WC approach) and "$_{ref}$" stands for a reference state.

2.2. Modelling the balance equations for rigid body transport

Body dynamics is ruled by Euler–Newton equations, whose discretization takes advantage from the SPH formalism and the coupling terms of Sections 2.3 and 2.4:

$$\begin{aligned} & \frac{d\underline{u}_{CM}}{dt} = \frac{\underline{F}_{TOT}}{m_B} \\ & \frac{d\underline{x}_{CM}}{dt} = \underline{u}_{CM} \\ & \underline{M}_{TOT} = \underline{\underline{I}}_C \frac{d\underline{\chi}_B}{dt} + \frac{d\underline{\underline{I}}_C}{dt}\underline{\chi}_B = \underline{\underline{I}}_C \frac{d\underline{\chi}_B}{dt} + \underline{\chi}_B \times \left(\underline{\underline{I}}_C \underline{\chi}_B\right) \\ & \quad \Rightarrow \frac{d\underline{\chi}_B}{dt} = \underline{\underline{I}}_C^{-1}\left[\underline{M}_{TOT} - \underline{\chi}_B \times \left(\underline{\underline{I}}_C \underline{\chi}_B\right)\right] \\ & \frac{d\underline{\alpha}}{dt} = \underline{\chi}_B \end{aligned} \tag{2.10}$$

where the subscript "$_B$" refers to a generic computational body and "$_{CM}$" to its centre of mass.

The first two relations of (2.10) represent the balance equations for the momentum and the time law for the position of the body barycentre ($\underline{F}_{TOT}$ is the global/resultant force acting on the solid). The last two formulas of the system express the balance equation of the angular momentum ($\underline{\chi}_B$ denotes the angular velocity of the generic body) and the time evolution of the solid orientation ($\underline{\alpha}$ is the vector of the angles lying between the body axis and the global reference system). $\underline{M}_{TOT}$ represents the associated torque acting on the body and $\underline{\underline{I}}_C$ the matrix of the moment of inertia of the computational body (Einstein's notation works for the subscript "$_l$"):

$$I_{c,ij} = \int_{V_B} \rho\left(r_l^2\delta_{ij} - r_i r_j\right)dV = \left\{ \begin{array}{c} \int_{V_B} \rho\left(r_k^2 + r_n^2\right)dV, i = j; k, n \neq i \\ -\int_{V_B} \rho\left(r_i r_j\right)dV, i \neq j \end{array} \right\} \tag{2.11}$$

In this sub-section $\underline{r}$ implicitly represents the relative distance from the body centre of mass.

In order to solve the system (2.10), we need to model the global force and torque, as described in the following. The resultant force is composed of several terms:

$$\underline{F}_{TOT} = \underline{G} + \underline{P}_F + \underline{T}_F + \underline{P}_S + \underline{T}_S, \quad \underline{T}_F + \underline{T}_S \cong 0 \tag{2.12}$$

$\underline{G}$ represents the gravity force, while $\underline{P}_F$ and $\underline{T}_F$ the vector sums of the pressure and shear forces provided by the fluid. Analogously, $\underline{P}_S$ and $\underline{T}_S$ are the vector sums of the normal and the shear forces provided by other bodies or boundaries (solid–solid interactions). As this study focuses on inertial and quasi-inertial fluid flows, we do not implement neither turbulence scheme nor tangential stresses (simplifying hypothesis). Future works are needed to extend the formulation of Section 1 to a wider category of fluid flows.

The fluid–solid interaction is expressed by the following pressure force:

$$\underline{P}_F = \sum_s p_s A_s \underline{n}_s \tag{2.13}$$

The computational body is numerically represented by solid volume elements, here called (solid) "body particles" ("$_s$"). Some of them describe the body surface and are referred to as "surface body particles". These particular elements are also characterized by an area and a vector $\underline{n}$ of norm 1. This is normal to the body face the particle (it belongs to) and points outward the fluid domain (inward the solid body).

We then implement the boundary treatment of Adami et al. [32] to compute the pressure of a body particle, as modified in Section 2.3. Further, the solid–solid interaction term ($\underline{P}_s$) is presented in Section 2.4.

On the other hand, the torque in (2.10) is discretized as the summation of each vector product between the relative position $\underline{r}_s$, of a surface body particle with respect to the body centre of mass, and the corresponding total particle force:

$$\underline{M}_{TOT} = \sum_s \underline{r}_s \times \underline{F}_s \tag{2.14}$$

Time integration of the equations in (2.10) is performed using a Leapfrog scheme analogous to and synchronized with (2.8). This means that the body particle pressure is computed simultaneously to fluid pressure, so that this parameter is staggered of around $dt/2$ with respect to all the other body particle parameters.

After time integration, we can obtain the velocity of a body particle as the sum of the velocity of the corresponding body barycentre and the relative velocity:

$$\underline{u}_s = \underline{u}_{CM} + \underline{\chi}_B \times \underline{r}_s \tag{2.15}$$

At this time, we can update the body particle normal vectors and absolute positions, according to the following kinematics formulas ($\underline{d\alpha}$ is the increment in the body rotation angle during the on-going time step and R_{ij} the body rotation matrix):

$$\begin{array}{l} \underline{n}_s(t+dt) = \underline{\underline{R}}_B \underline{n}_s(t), \quad \underline{x}_s(t+dt) = \underline{x}_{CM}(t+dt) + \underline{\underline{R}}_B \underline{r}_s(t) \\ \underline{\underline{R}}_B = \underline{\underline{R}}_x \underline{\underline{R}}_y \underline{\underline{R}}_z, \quad \underline{d\alpha}_B = \underline{\omega}_B dt \\ \underline{\underline{R}}_x = \begin{bmatrix} 1 & 0 & 0 \\ 0 & \cos\left(d\alpha_x\right) & \sin\left(d\alpha_x\right) \\ 0 & -\sin\left(d\alpha_x\right) & \cos\left(d\alpha_x\right) \end{bmatrix}, \\ \underline{\underline{R}}_y = \begin{bmatrix} \cos\left(d\alpha_y\right) & 0 & -\sin\left(d\alpha_y\right) \\ 0 & 1 & 0 \\ \sin\left(d\alpha_y\right) & 0 & \cos\left(d\alpha_y\right) \end{bmatrix}, \\ \underline{\underline{R}}_z = \begin{bmatrix} \cos\left(d\alpha_z\right) & \sin\left(d\alpha_z\right) & 0 \\ -\sin\left(d\alpha_z\right) & \cos\left(d\alpha_z\right) & 0 \\ 0 & 0 & 1 \end{bmatrix} \end{array} \tag{2.16}$$

2.3. Modelling the fluid–body interaction terms

The fluid–body interaction terms rely on the boundary technique introduced by Adami et al. [32], here implemented and adapted for free-slip conditions. If boundary is fixed, this method can be interpreted as a discretization of the semi-analytic approach used to treat fluid–boundary interactions (Section 2.1). The outer domain of (2.2) is here represented by all the body particles inside the kernel support of the computational fluid particle. Further, Adami et al. [32] introduces a new term, related to the acceleration of the fluid–solid interface, which influences the estimation of body particle pressure. The implementation and our modifications of this technique are hereafter described.

The fluid–body interaction term in the continuity equation represents a discrete approximation of the analogous term in (2.6), used to treat frontiers (free-slip conditions):

$$C_s = 2\rho_0 \sum_s [(\underline{u}_s - \underline{u}_0) \cdot \underline{n}_s] W'_s \omega_s \tag{2.17}$$

Analogously, the fluid–body interaction term in the momentum Eq. (2.7) assumes the form:

$$\underline{a}_s = \sum_s \left(\frac{p_s + p_0}{\rho_0^2}\right) W'_s m_s \tag{2.18}$$

The pressure value of the generic neighbouring surface body particle "$_s$" is derived as follows.

Let consider a generic point at a generic fluid–body interface. In case of free-slip conditions, the normal projection of the acceleration on the fluid side ("$_f$") and on the solid side ("$_w$") are equal (in-built motion in the direction normal to the interface):

$$\left(\frac{d\underline{u}_f}{dt}\right) \cdot \underline{n}_w = \left(-\frac{1}{\rho_f}\nabla p_f + \underline{g}\right) \cdot \underline{n}_w = \underline{a}_w \cdot \underline{n}_w \tag{2.19}$$

The "wall" acceleration at the position of a generic body particle can then be derived by linearizing (2.19). This depends on the particular computational fluid particle "$_0$" we are considering, so that we can refer to the interaction subscript "$_{s,0}$":

$$\begin{array}{l} \nabla p_f \cdot \underline{n}_w = \rho_f\left(-\underline{a}_w \cdot \underline{n}_w + \underline{g}\right) \cdot \underline{n}_w \Rightarrow p_{s0} \\ \qquad \approx p_0 + \rho_0\left(\underline{g} - \underline{a}_s\right) \cdot (\underline{x}_s - \underline{x}_0) \cdot \underline{n}_s \end{array} \tag{2.20}$$

One may apply a SPH interpolation over all the pressure values estimated according to (2.20) to derive a unique pressure value for a body particle:

$$p_s = \frac{\sum_0 p_{s0} W_{s0}\left(\frac{m_0}{\rho_0}\right)}{\sum_0 W_{s0}\left(\frac{m_0}{\rho_0}\right)} = \frac{\sum_0 \left[p_0 + \rho_0 \left(\underline{g} - \underline{a}_s\right) \cdot \underline{r}_{s0} \cdot \underline{n}_s\right] W_{s0}\left(\frac{m_0}{\rho_0}\right)}{\sum_0 W_{s0}\left(\frac{m_0}{\rho_0}\right)} \tag{2.21}$$

This pressure value is finally used in (2.18). The formulation provided by (2.17), (2.18) and (2.21) differs from Adami et al. [32] because of the presence of $\underline{n}_s$ in (2.21), necessary to represent free-slip conditions.

Let now consider that only a minority of the body particles represents the body surface, but we also need many inner body particles to estimate p_s. Thus, the model defines the normal vectors for the neighbouring body particles lying inside the bodies, as described by the following algorithm.

For any fluid–body particle interaction (Fig. 2.1, left panel), each fluid particle searches for the most representative surface body particle to define $\underline{n}_s$ in (2.21) – "$_{s0}$" interaction–. If the on-going body particle "$_s$" belongs to the body surface, then it is immediately considered as representative. Otherwise, the fluid particle "$_0$" isolates its visible neighbouring surface body particles. Visibility is assessed considering the sign of the projection of the inter-particle distance on the body particle normal. The visible neighbour, which is the closest to the joining segment of particles "$_0$" and "$_s$", is then selected. This particle provides the normal "$\underline{n}_s$" for the fluid–solid particle interaction "$_{s0}$" in (2.21).

We finally consider that the assumption (2.19) relies on the fact that all the involved variables are differentiable in time. This means that this equation cannot properly deal with impulses (infinite accelerations). However, the numerical accelerations of our model are always finite and the solid particle accelerations can be easily used in (2.21). Nevertheless, we prefer to define a maximum threshold for $|\underline{a}_s|$, here equal to 10 g.

Examples of the estimations of (2.21) are provided in Figs. 3.2(left) and 3.18(left).

2.4. Modelling the solid–solid interaction terms

The solid–solid interaction term in (2.12) – $\underline{P}_s$ – represents body–body and body–boundary (full elastic) impingement forces, whose time and spatial evolution, in the continuum, is theoretically proportional to the Dirac's delta. The numerical model needs to discretize $\underline{P}_s$ as explained hereafter.

The "boundary force particle" method of Monaghan [1] defines repulsive forces to represent a conservative full elastic impingement between two SPH interacting particles (of any medium). In particular, the acceleration $\underline{a}_{bfp,jk}$ of particle "$_j$", due to the impingement with particle "$_k$", is aligned with the inter-particle distance $\underline{r}$ and inversely proportional to its absolute value r:

$$\underline{a}_{bfp,jk} = \frac{f_{bfp}}{r_{jk}} \frac{m_k}{m_j + m_k} \underline{n}_{jk} \tag{2.22}$$

The analytic function f_{bfp} is symmetric with respect to the impact point. The dependence of (2.22) on the particle masses allows conserving both global momentum $\left(m_j \underline{a}_{bfp,jk} = -m_k \underline{a}_{bfp,kj}\right)$ and kinetic energy (one may notice that $\underline{n}_{jk} = -\underline{n}_{jk}$ and $f_{jk} = f_{kj}$). The formulation works for inter-particle high velocity impacts.

This formulation is here applied and extended to whole solid bodies (not only particle impingements), even at low velocities, as well as body–frontier interactions. Consider the overall force $\underline{P}_s$, which represents the impingements between a generic computational body ("$_B$") and all its neighbouring bodies ("$_K$") and frontiers ("$_{K^*}$"). $\underline{P}_s$ is decomposed in elementary 2-body ($\underline{P}_{BK}$) and body–frontier ($\underline{P}_{BK^*}$) interactions:

$$\underline{P}_S = \sum_K \underline{P}_{BK} + \sum_{K^*} \underline{P}_{BK^*} \tag{2.23}$$

Adopting the same principles of the boundary force particle method, $\underline{P}_{BK}$ involves interactions between all the body particles "$_j$" of the computational body "$_B$" and their neighbour body particles "$_k$", belonging to the neighbouring body "$_K$":

$$\underline{P}_{BK} = -\alpha_I \sum_j \sum_k \frac{2u^2_{\perp,jk}}{r_{per,jk}} \frac{m_j m_k}{m_j + m_k} \Gamma_{jk} \left(1 - \frac{r_{par,jk}}{dx_s}\right) \underline{n}_k \tag{2.24}$$

The components of the inter-particle relative distance, $\underline{r}_{par}$ and $\underline{r}_{per}$ (Fig. 2.1, centre panel), are parallel and perpendicular to the neighbour normal, respectively. The term within brackets in (2.24) deforms the kernel support of the body particles "$_j$", so that it mainly develops along the direction aligned with the normal of

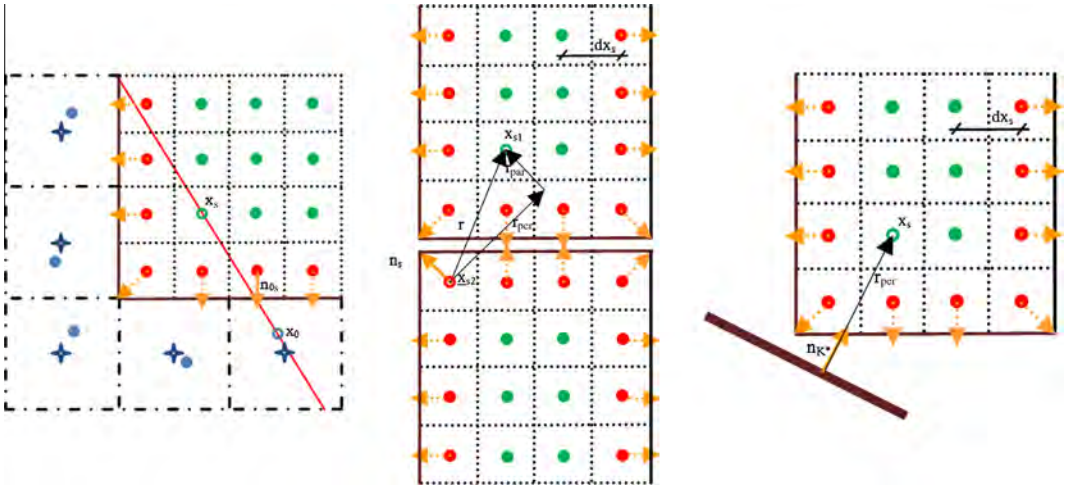

Fig. 2.1. Schematic representations of 2D non-homogeneous SPH interactions. Left panel: Detection of the normal $\underline{n}_{0s} = \underline{n}_s$ in the interaction of a generic inner body particle ($\underline{x}_s$) with a generic fluid particle ($\underline{x}_0$); red circles: barycentres of surface body particles; green circles: barycentres of the inner body particles; blue circles: numerical position of the fluid particles; blue crosses: barycentres of the fluid particles; dashed lines delimit the volume (surface in 2D) of the numerical elements; orange arrows: normal vectors of the surface body particles; continuous lines: body boundary. Centre panel: estimation of $\underline{r}$, $\underline{r}_{per}$ and $\underline{r}_{par}$ in the interaction between a generic inner body particle ($\underline{x}_{s1}$) and a generic surface body particle ($\underline{x}_{s2}$). Right panel: interaction of a generic inner body particle ($\underline{x}_s$) with a frontier "$_{K^*}$" (brown thick line). (For interpretation of the references to colour in this figure legend, the reader is referred to the web version of this article.)

the neighbouring particle (dx_s is the size of the body particles). The weighting function Γ is expressed according to Monaghan [1] and depends on $q = r_{jk}/h$:

$$\Gamma_{jk} = \begin{cases} \frac{2}{3}, & 0 \leqslant q < \frac{2}{3} \\ (2q - \frac{3}{2}q^2), & \frac{2}{3} \leqslant q < 1 \\ \frac{1}{2}(2-q)^2, & 1 \leqslant q < 2 \\ 0, & 2 \leqslant q \end{cases} \tag{2.25}$$

This study introduces two modifications for body–body interactions, with respect to the original formulation of the boundary force particles. The first one concerns the impact velocity $u_{\perp,jk}$, which replaces the term "0.1c" in the formulation of Monaghan [1] and properly deals with low velocity impacts. It avoids too strong or too weak impingement forces. For each body–body interaction, the impact velocity has a unique value for all the particle–particle interactions during the on-going time step. This velocity is computed as the maximum of the absolute values of the inter-particle relative velocity (projected over the normal of the neighbouring particle). For this purpose, the model considers all the inter-particle interactions recorded while the 2 bodies are approaching. The expression for the impact velocity reads:

$$u_{\perp,jk}(t) = \max_{j,k,t^*} \left\{ \left| \left[(\underline{u}_j - \underline{u}_k) \cdot \underline{n}_k \right] \right| \right\}, \quad t_0 \leqslant t^* \leqslant t \tag{2.26}$$

where t_0 refers to the beginning of the approaching phase. When other forces (e.g. pressure and gravity forces) are taken into account, the impact velocity can eventually increase in the inter-body impact zone, causing a potential and partial penetration of a solid into another body. In this case, and only during the approaching phase, (2.26) allows increasing the magnitude of the impingement force, depending on the actual impact velocity (instead of the undisturbed impact velocity). This modification avoids mass penetrations in case of complex impingements.

Further, this study introduces the coefficient α_I. This normalizing parameter corrects discretization errors and better preserves the global momentum and kinetic energy of the body–body system during the impingement. Neglecting α_I, (2.24) drastically under-estimates the impingement forces if the whole mass of the bodies does not lie within the impact zone (of depth 2 h). To avoid this shortcoming, a formulation for α_I is presented hereafter. Consider the absolute value of the impingement force P_s as a function of the global parameters of the bodies, instead of the particle values. This second formulation for P_{BK} is denoted as follows:

$$P_{BK}\prime \equiv \frac{2u^2_{\perp,BK}}{r_{per,BK}} \frac{m_B m_K}{m_B + m_K} \Gamma_{BK}, \quad r_{per,BK} = \min_{B,K} \{ r_{per,jk} \},$$
$$u^2_{\perp,BK} = \max_{B,K} \left\{ u^2_{\perp,jk} \right\} \tag{2.27}$$

The inter-body velocity impact $u_{\perp,BK}$ is now defined as the highest amongst the particle impact velocities, while the relative inter-body distance is considered as the minimum amongst the corresponding inter-particle distances. In practise, $u_{\perp,BK}$ can be roughly, but more efficiently, estimated as the sum of the absolute values of the two body particles, whose interaction shows the highest relative velocity in the system.

One may now derive a proper definition for α_I, by equalling P_{BK} to P'_{BK}:

$$\alpha_I = \sum_K \frac{u^2_{\perp,BK}}{r_{per,BK}} \frac{m_B m_K}{m_B + m_K} \Gamma_{BK} \Bigg/ \sum_j \sum_k \left[\frac{u^2_{\perp,jk}}{r_{per,jk}} \frac{m_j m_k}{m_j + m_k} \Gamma_{jk} \left(1 - \frac{r_{par,jk}}{dx_s} \right) \right] \tag{2.28}$$

In practise, we prefer to use the following approximated formulation to speed-up the simulations:

$$\alpha_I = \sum_K \frac{1}{r_{per,BK}} \frac{m_B m_K}{m_B + m_K} \Gamma_{BK} \Bigg/ \sum_j \sum_k \left[\frac{1}{r_{per,jk}} \frac{m_j m_k}{m_j + m_k} \Gamma_{jk} \left(1 - \frac{r_{par,jk}}{dx_s} \right) \right] \tag{2.29}$$

(2.29) is equivalent to considering the body impact velocity as a weighted average of the particle impact velocities of (2.23).

At a first approximation, the normalizing factor α_I roughly represents the inverse of the fraction of the system mass which lies into the impingement zone. This mass should numerically represent the 2-body system during the impact. On the other hand, one cannot use (2.27) to model a body–body impact. In this case, for example, a definition for the direction of P'_s is required, but the direction of the relative distance between the two bodies does not avoid mass penetration. This would happen, for example, if two cubic bodies, very close to each other and with null barycentre velocities, began to rotate.

Finally, the model represents body–boundary interactions. A generic boundary is modelled as a body with infinite mass and discretization tending to zero (the semi-analytic approach, used to model frontiers, is an integral method). The interaction force assumes the following expression (here the subscript "$_{K^*}$" refers to a generic neighbouring frontier; Fig. 2.1, right panel):

$$\underline{P}_{BK^*} = -\alpha_I \sum_j \frac{2u^2_{\perp,jK^*}}{r_{per,jK^*}} m_j \Gamma_{jK^*} \underline{n}_{K^*}, \quad \alpha_I = \frac{m_B}{r_{per,BK^*}} \Gamma_{BK^*} \Bigg/ \sum_j \left(\frac{m_j}{r_{per,jK^*}} \Gamma_{jK^*} \right) \tag{2.30}$$

2.5. Model algorithm

This section briefly reports the main features of the model algorithm (Fig. 2.2).

The parameters of the fluid particles, the body particles and the domain frontiers are directly initialized in input, depending on the test case. This simple process generally does not require relevant efforts, especially if a discretized boundary geometry is already available. The initial fluid volume/s are assigned as one/more fluid polyhedron/s. Uniform-sized SPH fluid particles fill this volume/s and are located on Cartesian grids, which are cut by the polyhedron faces. The fluid domain can assume any generic 3D shape (the

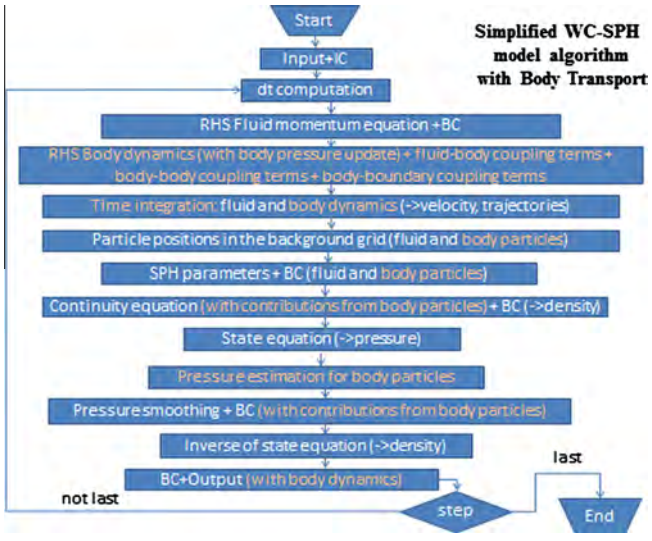

Fig. 2.2. Simplified algorithm of the numerical model. In orange we highlight the numerical features developed during this study to allow representing the transport of solid bodies in free surface flows. (For interpretation of the references to colour in this figure legend, the reader is referred to the web version of this article.)

initial positions of the SPH fluid particles are not exactly optimized to minimize the SPH truncation errors). At this stage, only density is evaluated from the initial pressure values, using the inverse of the state equation. Each 3D solid body is completely discretized with uniform-sized body particles, disposed on a regular Cartesian grid in the local reference system of the body. This procedure has been applied to geometries represented by Boolean operations over parallelepiped/rectangle shapes, such as the 2D and 3D bodies simulated in Section 3. The application of the presented model on more complex 3D body geometries is quite straightforward. It would eventually require an optimized procedure to initialize particle positions inside the bodies and further validations. Contrarily, fixed frontiers do not need any discretization, according to the semi-analytic approach [33].

At the beginning of any iteration, we assess the time step duration. We then compute the Right Hand Sides (RHS) of the particle balance equations for the fluid momentum, with the corresponding boundary conditions at frontiers ("semi-analytical approach"). Further, we estimate the RHS of the body dynamics equations, with the fluid–body, body–body and body–boundary coupling terms. It follows time integration for all the cited equations and we get fluid/body particle velocities and trajectories. At this point, we associate particles with the cells of a coarse reference/background (non-computational) grid. This way, we can efficiently compute all the geometrical parameters needed by the SPH technique (relative distances, kernel functions and derivatives, Shepard coefficient, neighbouring lists). The model can now estimate fluid density by solving the continuity equation (with the fluid–body coupling terms) and convert it into pressure, through the state equation (WC approach). At this stage, the model estimates the pressure values of the surface body particles. The fluid pressure field is then partially smoothed (according to Di Monaco et al. [33] and Areti et al. [52]) and converted again in a density field. Finally, the model checks boundary conditions and eventually writes output files.

3. Results

After some preliminary investigations (flat body impinged by a water jet – Section 3.1, body–body and body–boundary impacts – Sections 3.2 and 3.3), the numerical model presented in Section 2 is validated on a sequence of four 2D test cases involving water entries of falling wedges (Section 3.4). Further, the model is tested when dealing with simultaneous multiple interactions (fluid–body, body–body and body–boundary – Section 3.5), just to verify that no mass penetration occurs during multiple 3D impingements. We then validate the model performance over a dam break event (Section 3.6), involving the 3D transport (6 degrees of freedom) of a floating body, a moving dam/gate (treated as a body in terms of fluid–body interactions) and fixed obstacles (treated as frontiers). A similar case is finally explored to provide a demonstrative 3D test with the simultaneous transport of 9 solid bodies during a dam break event.

For each of the following test cases, we set $h/dx = 1.3$ and the CFL number to 0.1. If not otherwise stated, the present model will be denoted by "SPH-body", just for simplicity of notation.

3.1. Flat body impinged by a water jet (2D)

This test case provides a validation of the fluid–body interaction scheme, at high velocity impacts. A water jet perpendicularly impinges a flat body (gravity effects are negligible). The jet inlet section is characterized by the diameter $D = 0.028$ m and the absolute value of velocity $|\underline{u}_{in}| = 19.61$ m/s. The flow can be approximately considered as potential [53]. The distance between the inlet section and the body surface is 0.120 m. The particle size is $dx = 0.001$ m and $dx/dx_s = 2.0$. After $t = 0.1$ s, stationary conditions are approximately established. At this time, Bernoulli's theorem can be applied to derive an analytical solution [53]. The field of the pressure coefficient is characterized by its maximum value (equal to unity) at the stagnation point, where kinetic energy is zero, and null values far from the plate, where the kinetic energy tends to the total energy. These conditions are numerically well represented in Fig. 3.1(left), where the pressure coefficient is defined as $C_p \equiv \left(p/0.5\rho|\underline{u}_{in}|^2\right)$, despite some overestimations over the body surface, around the stagnation point.

A quantitative validation is provided in Fig. 3.1 (right). The numerical model well reproduces the spatial evolution of the pressure coefficient, even if it slightly over-predicts the peak of the pressure coefficient (of around 10%). Nevertheless its performance is satisfying, especially when compared with other the SPH boundary techniques like the semi-analytic approach ("SA-SPH", as described in Di Monaco et al. [33] and validated on this test case in Amicarelli et al. [39]). At the same time, the boundary treatment relying on discrete surface boundary elements ("DB-SPH", presented in Amicarelli et al. [39]) provides better results. The differences between the three SPH methods compared in Fig. 3.1(right panel) are briefly discussed in the following.

The Discrete Boundary (DB)-SPH approach [39] relies on a complete SPH particle approximation with both volume and surface terms [35], uses discrete wall elements and adopts an upwind first order spatial reconstruction scheme at boundaries, based on a Linearized Partial Riemann Solver [17]. Although a better accuracy attained by the DB-SPH approach on this test case, the scheme defined in Section 2.3 (named "SPH-body" in Fig. 3.1) was implemented and validated for the fluid–body interactions of the

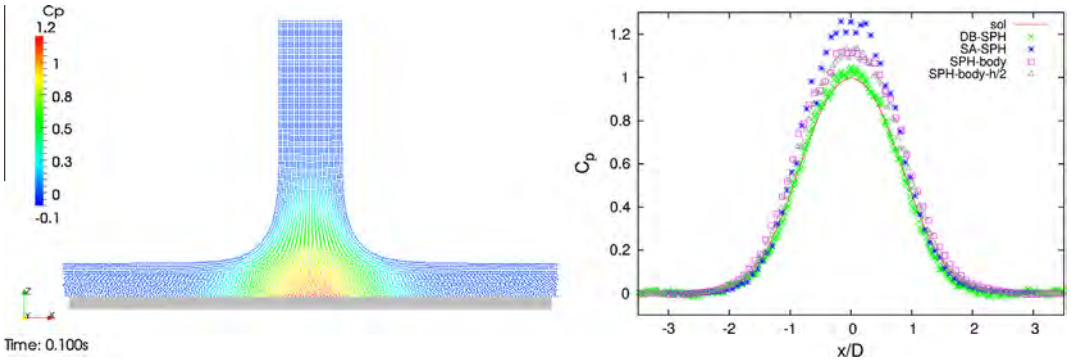

Fig. 3.1. Flat body impinged by a water jet. Left panel: field of the pressure coefficient under stationary conditions (body particles are coloured in semitransparent black). Right panel: profile of the pressure coefficient over the plate; comparison between the model results ("SPH-body"), the analytical solution ("sol"; [53]), a simulation with a halved h value ("SPH-body-h/2") and other SPH results ("SA-SPH" and "DB-SPH", as reported in Amicarelli et al. [39]). (For interpretation of the references to colour in this figure legend, the reader is referred to the web version of this article.)

presented model (Section 3). Contrarily to DB-SPH method, the approach of Section 2.3 requires a simpler and faster algorithm, does not alter the mathematical model of Section 2.1 in the inner domain and efficiently benefits of the presence of the body particles, which are however required by the presented model to compute the time-dependent moments of inertia of the solid bodies (Section 2.2).

SA-SPH method represents a semi-analytical approach [34,33], which fills the truncated part of a boundary kernel with a fictitious "outer volume", where analytical integrals are computed. The simplifying hypothesis on the fluid dynamics fields in the "outer domain" limits its performance on this test case. However, SA-SPH approach still provides valuable results in 3D SPH modelling (e.g. [33,39]) and is here used for fluid–frontier interactions (one may notice in Section 1 that frontiers are neither considered as solid bodies, nor discretized with body particles).

Considering a further simulation of the presented model with a halved kernel support length ("SPH-body-h/2"), the reference results ("SPH-body") show sufficiently independent from spatial resolution (Fig. 3.1, right panel).

Finally, Fig. 3.2 reports some details of the fields of the pressure coefficient (left panel) and the absolute value of velocity, scaled on the inlet velocity (right panel). In the first image the body particles are coloured according to their pressure coefficient values. The resulting pressure field depicted by the values of the body particles is regular and well matches the fluid pressure field at the fluid–solid interface. Further, particles without fluid neighbours keep null pressure values. In the latter image (right) we also verify that the present boundary treatment (Section 2.2) avoids penetration of fluid particles into the solid plate (body particles are coloured in semitransparent black so that any eventual penetration would be clearly visible).

3.2. 1D body–body impingements of 3D solids

These test cases reproduce several elementary and full elastic 2-body impingements (gravity is neglected). The test cases are 3D, even if the impact dynamics are 1D. This section provides a preliminary validation of the numerical scheme of Section 2.4. (modified version of the "boundary force particles")

Three configurations are explored: a symmetric case ("sym", with absolute value of velocity equal for both the bodies) and two asymmetric test cases, with alternatively high ("high_vel") and low ("low_vel") impact velocities, as explained in the following.

We set $dx_s = 0.0025$ m and bodies are cubes of 0.05 m length. In the first case the initial absolute value of velocity $|\underline{u}_{CM}|$ for both the bodies is 0.5 m/s; the body velocities are 0.25 m/s and 0.75 m/s in the second test, while the third configuration considers lower values (0.025 m/s and 0.075 m/s).

Fig. 3.3(left column) shows a sequence of the velocity field (u) in case of low velocity impact ("low_vel"). The bodies begin to interact (top), collide at null velocities (centre) and leave the impact zone (bottom). Their absolute values of the simulated body velocities at the end of the interaction are correctly exchanged, with respect to the initial conditions (conservation of the global momentum and kinetic energy). The errors are beyond the 9th significant digit and are only caused by numerical truncation errors. When the bodies collide, they are not exactly touching. A very thin space (of the order of dx_s) guarantees that, even in more complex configurations, like full 3D interactions in presence of water, boundaries and gravity, no penetration occurs (let consider that the SPH spatial resolution is defined as 2 h or 4 h, instead of dx_s).

The time evolution of velocity is reported in Fig. 3.3 (top right panel). Hereafter, we normalize time on the impact time, simply defined as the whole interaction period. Each curve is correctly symmetric with respect to $t = t^* = 0.5$. Further, once having normalized the velocities on their initial values, the curves of the low velocity case and the ones of the asymmetric case (at higher velocities) overlap each other. This represents some simple numerical evidence that the model performance is not sensitive to the impact velocity.

When normalizing the curves of the absolute value of the interaction forces for all the six bodies (in the three different simulations), they all overlap each other (Fig. 3.3, bottom right panel). In particular, they are similar to Gaussian functions (with peaks at the minimum relative distance) and keep symmetric with respect to $t = t^* = 0.5$. These curves represent discrete approximations of Dirac's delta function, which theoretically relates to the time evolution of an impulse force.

Finally, the formulation presented in Section 2.4 allows representing elementary full elastic 2-body impacts with no mass penetrations, even at low velocities.

3.3. 1D body–boundary interactions for a 3D solid

According to the procedure explained in Section 3.2., we here validate a simple body–boundary interaction, according to (2.30). The numerical parameters of the body are the same as the previous test case, but the initial absolute value of the body velocity is alternatively equal to 1.0 m/s ("high_vel") or 0.10 m/s ("low_vel"). On the other side, the boundary is fixed.

A sequence of the field of the absolute value of velocity is reported in Fig. 3.4 (left column). The black line represents the solid boundary (lateral view). The impact zone, with depth of 2 h, lies between this line and the violet one.

The time evolution of the absolute value of velocity (Fig. 3.4, top right panel) is symmetric with respect to the impact time ($t = t^* = 0.5$), when the body velocity is null. The initial and final values of the body velocity are exactly equal (but for truncation

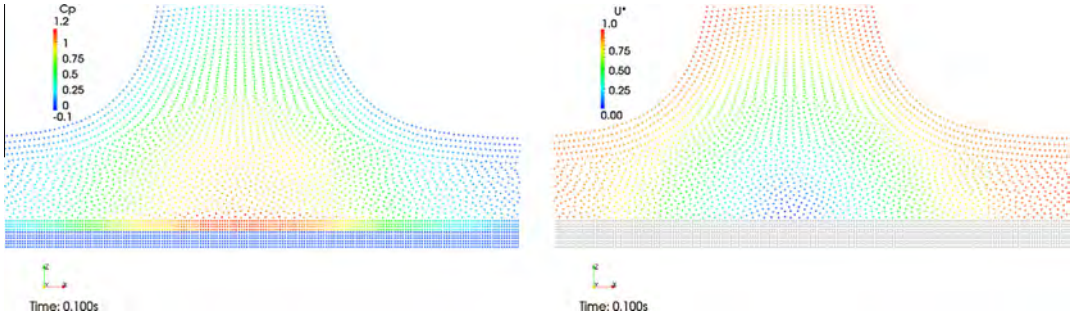

Fig. 3.2. Flat body impinged by a water jet. Left panel: details of the field of the pressure coefficient over the body surface (body particle values are shown). Right panel: details of the field of the absolute value of velocity (scaled on the inlet velocity; body particles are coloured in semitransparent black). (For interpretation of the references to colour in this figure legend, the reader is referred to the web version of this article.)

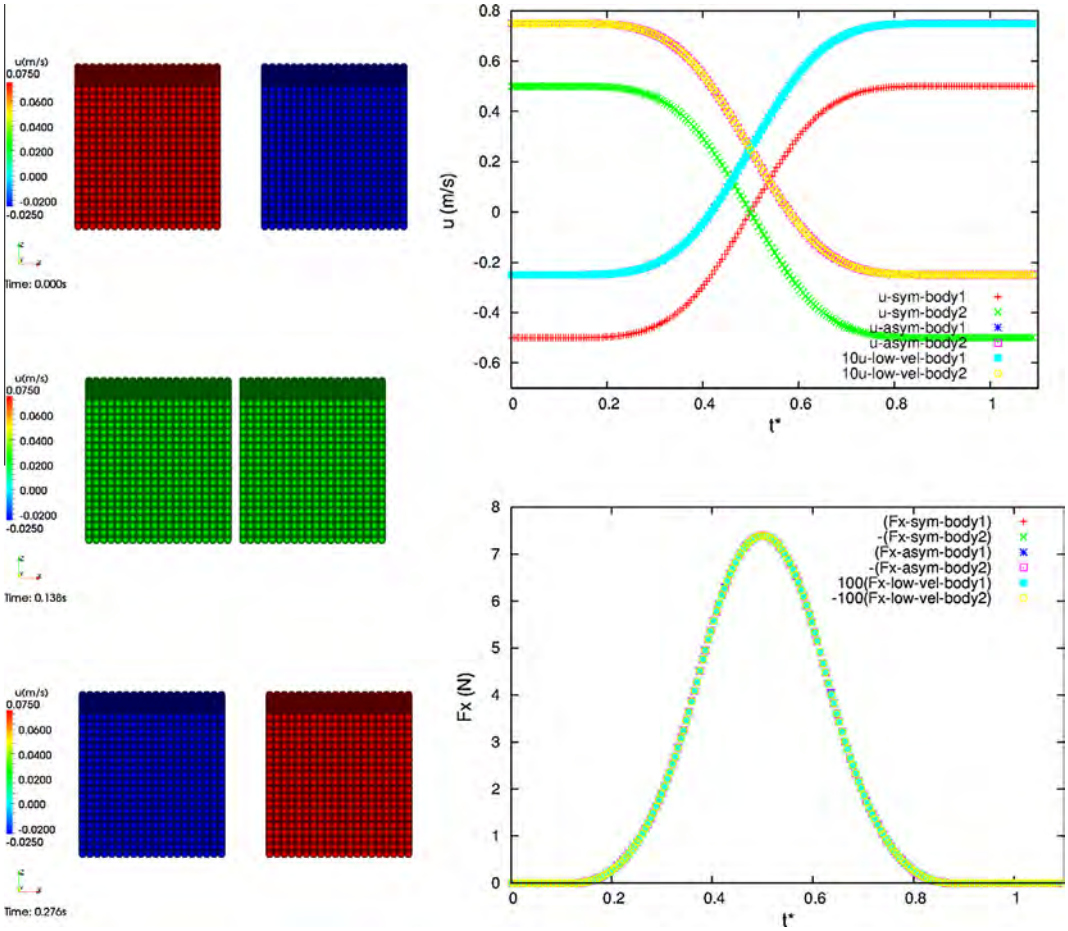

Fig. 3.3. 1D body–body impacts of 3D solids. Left column: sequence of the velocity field for the low velocity impact ("low_vel"). Right column: time evolution of the x-component of velocity for all the test cases (top panel) and absolute value of the interaction force for all the test cases (bottom panel).

errors beyond the 9th significant digit) providing the solution for a full elastic impact. The curves of the two simulations overlap, once scaling both velocity and time.

Analogously to what happens in body–body impacts, the impingement is represented as a continuous dynamics ruled by an interaction force derivable in time (Fig. 3.4, bottom right panel). Validation shows that the reliability of this representation does not depend on the impact velocity.

3.4. Water entries of falling wedges (2D)

The numerical model of Section 2 is tested on a sequence of four experimental test cases [54], involving water entries of falling wedges (2D). These represent equivalent bodies so that the model can directly represent only their portions interacting with water (triangles as in Fig. 3.6). The effects caused by the rest of the body are taken into account by considering the whole mass and moment of inertia and the actual centre of mass, located outside the numerical body (in brown in Fig. 3.6). Full details of the experimental set-up are provided in Hay et al. [54]. The four test cases differ from each other in terms of mass, moment of inertia, initial position and body orientation (with respect to the free surface), as reported in Table 3.1. Experimental measures and numerical inter-comparisons are available for all the test cases. The initial velocities and positions refer to the wedge as it is experimentally represented. As we just perform a single phase simulation, we consider that, before the impact with water, wedges are simply accelerated by gravity. This hypothesis introduces some discrepancies with respect to the experiments, mainly in terms of initial conditions of the very numerical simulations, which start at the impact time (t_{imp}, provided as an experimental input). Further, for the symmetric cases, the time origin has been translated of the same value for both the experimental and numerical curves, so that the impact time is simply set to zero. The base of the triangular wedges (Fig. 3.6) is $L = 0.610$ m, their height $H = 0.111$ m. The origin of the reference system is located where the lowest point of the triangle touches the free surface (Fig. 3.6, top left panel), at $t = t_{imp}$. The numerical simulations adopt $dx = 0.002$ m and $dx/dx_s = 2.0$.

Even though the impact time is an experimental input, some minor discrepancies still survive in terms of numerical initial conditions. In fact, our mono-phase approach determines an impact velocity of -3.4588 m/s and the wedge orientation should not change during the fall. We cannot replace this data with the experimental one, because this is not available. Even if this lack of information can be appreciable, its effect is clearly detectable and does not disturb these model validations, as demonstrated in the following subsections.

Validations are performed against experimental results [54] in terms of vertical acceleration, normalized by the gravitational one (a/g), and angular acceleration, expressed in 10^3 deg/s^2. Further inter-comparisons are provided for the maximum values of pressure on the wedge surface, taking into account the URANS results of Hay et al. [54]. The acceleration computed for the symmetric test cases is also compared with the estimations provided by a theoretical method (the asymptotic method of Hay et al. [54]).

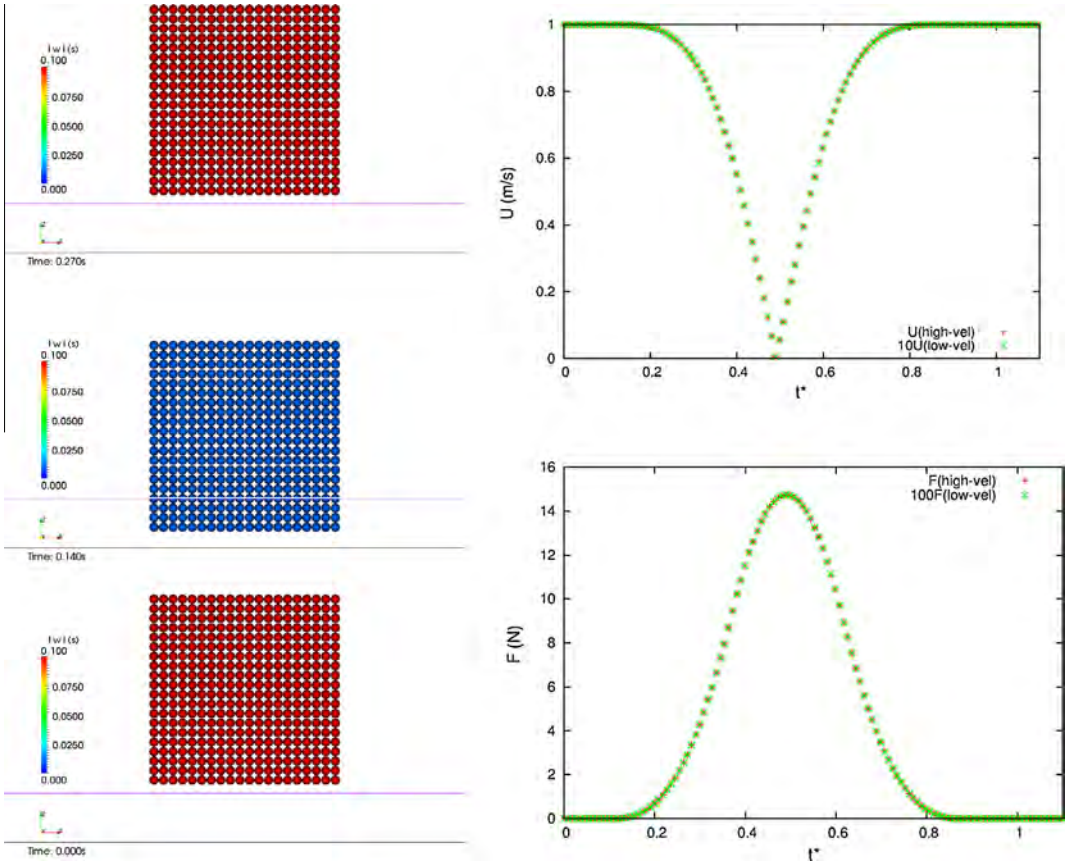

Fig. 3.4. 1D body–boundary impacts for a 3D solid. Left panel: sequence of the field of the absolute value of velocity (lateral view; "low_vel" case). Right column: time evolution of the x-component of velocity (top panel), and the absolute value of the interaction force (bottom panel).

Table 3.1
Synoptic view of the experimental parameters for the four test cases involving falling wedges [54].

Test case	$z_{CM}(t_0, m)$	m_B (kg/m)	I_c (kg $*$ m)	Heel angle (t_0)	t_{imp} (s)
Symmetric water entry, light (weight) wedge	0.216 + 0.610	50.000	/	0°	0.000
Symmetric water entry, medium (weight) wedge	0.216 + 0.610	119.262	/	0°	0.000
Asymmetric water entry, light (weight) wedge	0.216 + 0.610	50.820	3.6270	5°	0.356
Asymmetric water entry, medium (weight) wedge	0.165 + 0.610	120.080	4.4877	5°	0.355

Hereafter, experimental errors are not shown in case they were treated as negligible by the associated authors. On the other hand, SPH truncation errors are represented by error-bars, whose length is roughly overestimated by treating errors as instantaneous fluctuations around the reference time-averaged values.

3.4.1. Symmetric water entry of a light wedge (2D)

Time evolution of the normalized acceleration is reported in Fig. 3.5(left column). At the impact time ($t = 0$ s), only gravity forces are acting on the numerical body ($a/g = -1$). As the wedge crosses the free surface, the hydrodynamic vertical force grows until a maximum (at around 0.008 s) and then exponentially decreases, while the velocity of the body decelerates as well. The numerical results show a good agreement with the experimental values, in terms of time evolution, peak value and absolute errors. At the same time some differences can be appreciated. The numerical evolution is smoother than the experimental one and the initial conditions are not exactly the same. The first issue mainly concerns the solid deformation: the experimental body has a finite stiffness, so that its very small deformations cause some small-scale pressure oscillations in the fluid domain, propagating from the solid–fluid interface. They cannot be represented in the frame of rigid solid simulations Xu et al. [55]. As we numerically treat bodies with infinite stiffness, we filter these small scale oscillations, whose representation is beyond the aim of this study. In this context, a secondary source of error could be introduced by treating inertial flows, without modelling any turbulent shear stress (no contributions of turbulent vortices, which are formally smaller than 2 h or 4 h).

The second minor discrepancy (initial conditions) is due to the solid-air interactions before the impact (as already discussed at the beginning of Section 3.4; mono-phase formulation).

We also notice that our SPH results are in agreement with the estimations provided by a theoretical method (asymptotic method of Hay et al. [54]), which provides an approximated and smooth solution.

A more complex estimation is represented by the time evolution of the C_p maximum value (Fig. 3.5, right panel; the velocity scale is here the impact velocity). C_p is null at the beginning of the simulation, reaches a maximum of around $C_p = 16$ at $t = 0.002$ s (much sooner than the maximum value of the resultant force) and then exponentially decreases until the end of the

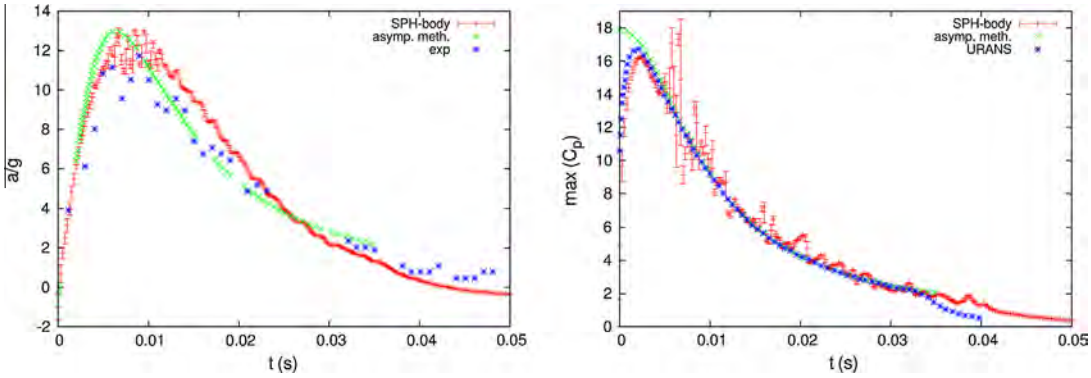

Fig. 3.5. Symmetric water entry of a light wedge. Left panel: time evolution of the normalized acceleration. Right panel: time evolution of the maximum value of the pressure coefficient over the wedge surface. Validation and inter-comparisons.

simulation, showing a somewhat noisy behaviour. SPH models usually suffer from some spurious very small-scale perturbations of the pressure field, and normally show some appreciable errors in computing the highest and lowest particle values of pressure. Further, we here estimate the very highest C_p value amongst all the boundary particles at the interface solid–fluid (100th percentile). Despite these general difficulties, we can appreciate the reliability of the present model in computing the maximum values of the pressure levels, by comparison with URANS estimations of Hay et al. [54] (Fig. 3.5, right). For further inter-comparisons, the asymptotic method provides a theoretical solution, whose initial conditions do not satisfy the constraint $C_p = 0$. After $t = 0.002$ s, this theoretical and approximated curve begins to be very close to the experimental and the numerical ones. One may notice that the model accuracy depends on the choice of the artificial speed of sound in (2.9). For the test cases of Section 3, working with maximum values of the Mach number at around Ma = 0.1 (upper limit imposed by any Weakly Compressible CFD approach), guarantees the result accuracy.

We can analyse the fields of the pressure coefficient in Fig. 3.6(left column) and compare them with the analogous simulation of Section 3.6.2, which considers a heavier wedge (Table 3.1).

The impact defines the beginning of the numerical simulation ($t = 0$ s). For both cases, the highest value of the maximum C_p is roughly reached at around $t = 0.002$ s. The peak of the hydrodynamic force occurs at around 0.008 s and 0.016 s for the light and medium wedge, respectively. The medium weight wedge is clearly faster than the light one. Thus, the maximum value of the hydrodynamic force is higher, delayed in time and occurs when more than a half of each lateral side of the wedge interacts with water. At $t = 0.030$ s, the whole bottom surface of the medium wedge is completely inside the inner fluid domain, whilst the light wedge is still higher on the free surface and its lateral vertices are just covered by a very thin layer of fluid. This is represented by the two lateral and symmetric jets, which are generated after the impact. They move along the bottom sides of the wedges and keep these directions even when they leave the fluid–solid interfaces. When the bottom sides of the light wedge are completely submerged ($t = 0.042$ s), the medium wedge is still lower and its lateral jets are no longer aligned with the bottom sides of the body. At this time, they directly interact with the water reservoir and are deflected upward.

Fig. 3.7 finally provides some examples of the field of the normalized velocity. The relative maxima are recorded along the vertical lines passing for the lateral vertices of the wedge, while the lateral jets present the absolute highest values of velocity. As for Fig. 3.6, the body is coloured in semitransparent black, so that we can appreciate that no fluid particle crosses the fluid–body interface, thus no mass penetration occurs.

3.4.2. Symmetric water entry of a medium weight wedge (2D)

This test case mainly differs from the previous one in terms of wedge mass, which is approximately 2.4 times heavier than the light wedge case (Table 3.1). We have analyzed the pressure and velocity fields in Section 3.4.1 and we here quantitatively validate the corresponding results.

The time evolution of the normalized acceleration is analogous to the one of the light wedge (Fig. 3.8, top left panel). Here the maximum value of a/g is reached later, at around $t = 0.016$ s. The comparisons with experimental results reveal a good performance of the model, both in terms of time evolution and peak values. At the same time some minor discrepancies are recorded. The experimental data show a noisier evolution than SPH results and initial conditions do not match exactly. These minor discrepancies are due to the use of rigid bodies and a mono-phase approach, respectively (as explained in Section 3.4.1). Further, all the numerical results lie within 36% of the approximated and theoretical estimations of the asymptotic method [54].

Fig. 3.8(top right panel) shows the time evolution of the maximum value of the pressure coefficient on the wedge surface. Despite some noise in its shape, SPH results agree quite well with the URANS estimations Hay et al. [54], both in terms of general trend and peak levels. A further inter-comparison is still provided by the theoretical and approximated solution of the asymptotic method.

Fig. 3.8(bottom) reports in detail an example of the field of the pressure coefficient. At this scale, we can better appreciate the spatial evolution of the pressure field at $t = 0.030$ s, when the bottom sides of the wedge begin to be completely submerged. The peak occurs below the lateral vertices of the body and pressure levels decrease towards the bottom vertex of the body. The pressure field is quite regular and no relevant spurious oscillations are observed. Finally, we notice that no fluid particle penetrates the solid domain (here coloured in semitransparent black).

3.4.3. Asymmetric water entry of a light wedge (2D)

The test cases analyzed in the present and the next sub-section provide further validations in terms of body accelerations and pressure maxima. At the same time, they evaluate the performance of the model in estimating the angular acceleration of solid wedges falling into a water pool.

The main difference, with respect to the symmetric wedge falls, consists in the initial orientation of the body with respect to the free surface. The angle between the body axis (which passes for the centre of the top side) and the vertical axis is 5° (heel angle). During the experimental realization, the pressure values become positive even before the impact, because of some air cushioning effects Hay et al. [54], as also denoted by the gradient of the first part of the experimental curve in Fig. 3.9(top, left panel).

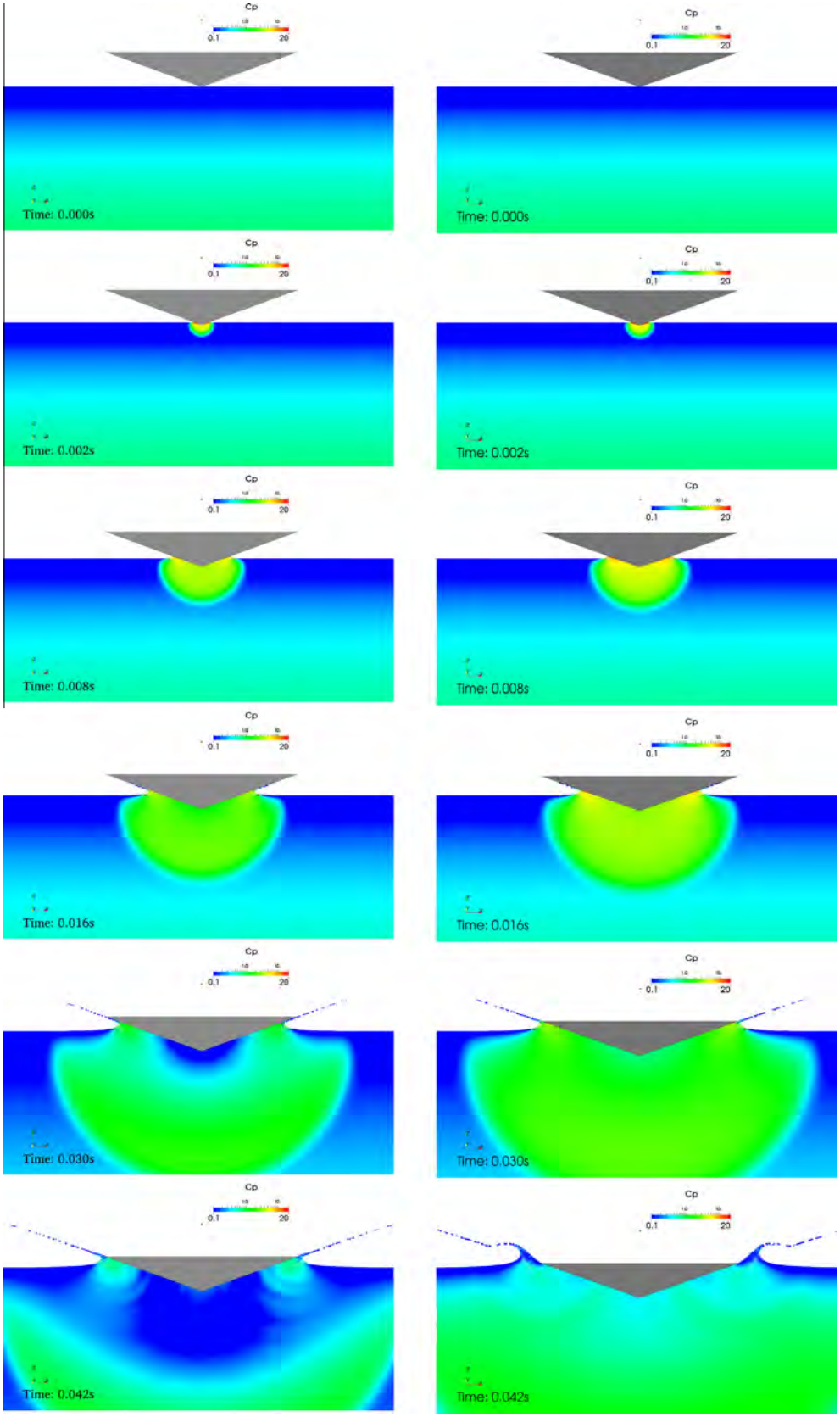

Fig. 3.6. Symmetric water entries of solid wedges: time evolution of the field of the pressure coefficient. Left column: light wedge. Right column: medium wedge.

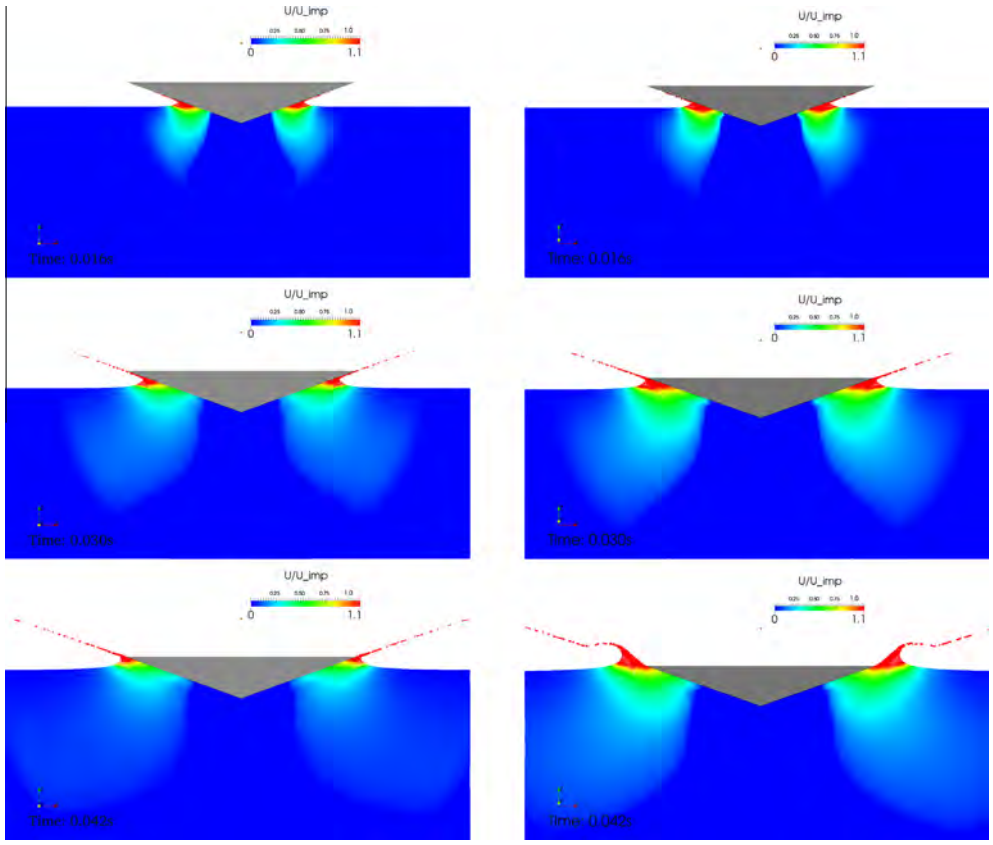

Fig. 3.7. Symmetric water entries of solid wedges: time evolution of the field of the absolute value of the normalized velocity. Left column: light wedge. Right column: medium wedge.

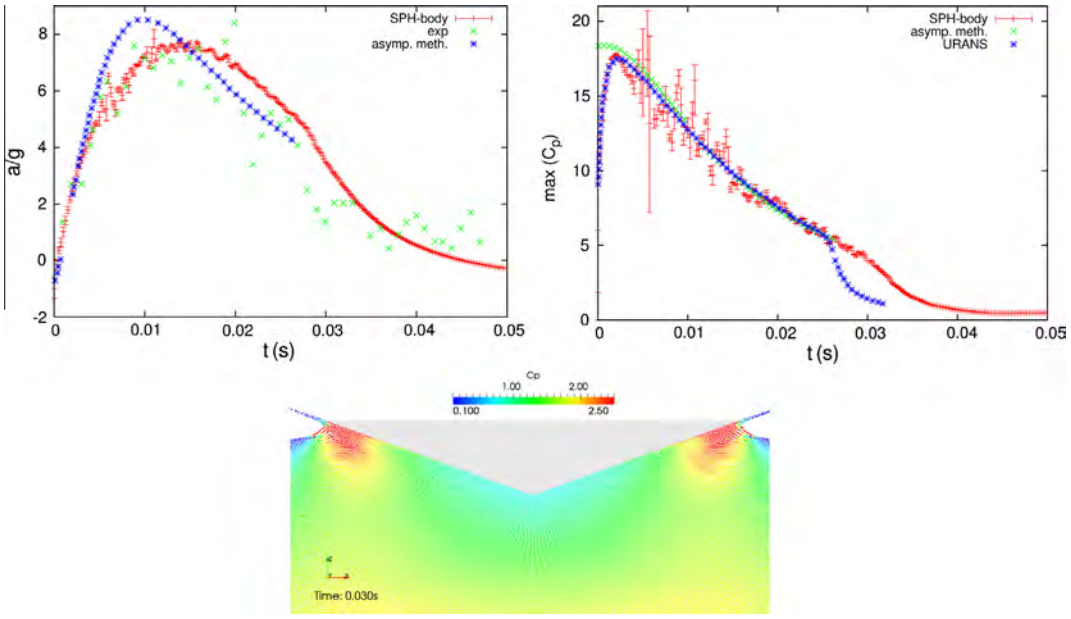

Fig. 3.8. Symmetric water entry of a medium (weight) wedge. Top. Left panel: time evolution of the normalized acceleration. Right panel: time evolution of the maximum value of the pressure coefficient over the wedge. Bottom panel: example of the field of the pressure coefficient. Validation and inter-comparisons.

According to the experimental data, the impact time should be $t = 0.356$ s. The same figure shows the comparison between the SPH results and the experimental values. The agreement is satisfying, both in terms of time evolution and peak value. The minor discrepancy, related to the initial conditions, has the same cause discussed in the previous sub-sections (mono-phase approach). Further, we notice some underestimation of the force in the last phase of the simulation.

The time evolution of the angular acceleration is reported in Fig. 3.9(top, right). The numerical model provides a good

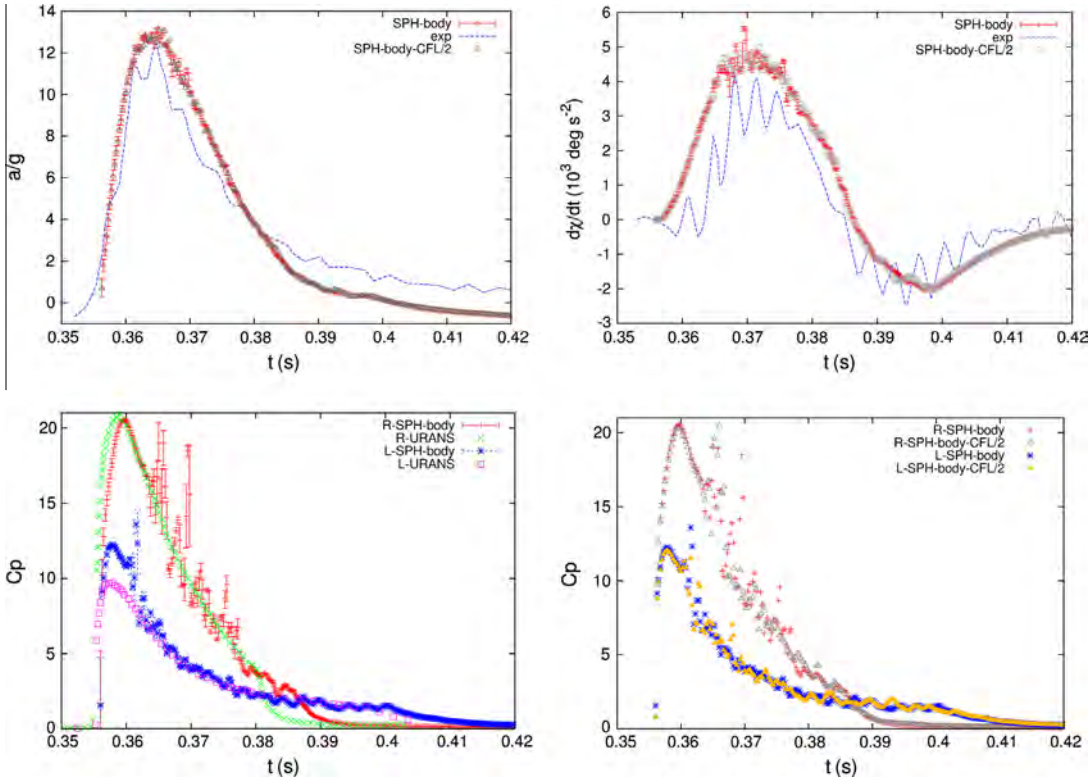

Fig. 3.9. Asymmetric water entry of a light wedge. Top. Left panel: time evolution of the normalized acceleration. Right panel: time evolution of the angular acceleration. Bottom panel: time evolution of the maximum value of the pressure coefficient over the wedge surface. Validation and inter-comparisons. The reference simulation is also performed at a halved CFL number ("SPH-body-CFL/2").

estimation of this parameter, which is more sensitive to the effects of the body deformability (experimental small scale oscillations) than the linear acceleration. The SPH curve should then be interpreted as a filtered estimation of the measured profile. As for the previous test cases, the lack of experimental data causes some discrepancies in the first stage of the simulation, which is mono-phase. This statement can be supported by two considerations. First, the highest error in the time pattern of the angular acceleration occurs at the impact. At this time the numerical body begins to rotate anticlockwise, whilst the experimental one has been already rotating on the other sense for few instants. In fact, air cushioning effects are not numerically modelled. In this context, we remind that the body centre of mass is outside and higher than the modelled wedge (Table 3.1). Secondly, some evidence may arise in Section 3.4.4 (asymmetric medium wedge), when the SPH numerical estimation of the angular acceleration is noticeably more reliable and there is no systematic estimation in the first part of the simulation. In fact, the dynamics of a heavier body is less sensitive to air–solid interactions. Considering a further simulation of the presented model with a halved CFL number ("SPH-body-CFL/2"), the reference results ("SPH-body") show sufficiently independent from time stepping (Fig. 3.9, top row and bottom right panels). We finally notice that the light body is more dependent on the slight overestimation in the peaks of the pressure levels at the beginning of the simulation, reproduced on the left side of the wedge, as described hereafter.

Fig. 3.9(bottom panels) shows the maximum values of the pressure coefficient, by comparing the SPH results with the URANS estimations of Hay et al. [54]. The peak in the left side of the wedge ("L") introduces a fictitious contribution, which tends to rotate the wedge anticlockwise. On the other hand, time evolution of the peak values in the right ("R") side of the wedge are satisfactorily reproduced, apart from some small scale noise.

A time sequence of the field of the pressure coefficient is represented in Fig. 3.10(left column), in comparison with the analogous test case of Section 3.4.4 (asymmetric medium wedge, right column). The light wedge reaches the maximum value of C_p on its left bottom side at around $t = 0.357$ s, just before the peak is recorded on the curve of the right bottom side of the wedge (at around $t = 0.359$ s). As the wedge enters the water pool, the overall hydrodynamic force increases up to a maximum value (at around $t = 0.365$ s). During this first phase the body has been increasingly accelerated in its anticlockwise rotation up to a maximum provided at around $t = 0.371$ s.

After this time, both the vertical force and the torque decrease together until around $t = 0.385$ s. Now the angular velocity of the body begins to decrease as the contributions to the torque, as applied on the left side of the wedge, become predominant with respect to the right side (even if the body will never rotate clockwise). Two jets are already visible, as the free surface is deviated by the wedge itself. These jets have the same orientation of the wedge bottom sides. The maximum value of the clockwise angular acceleration is reached at around $t = 0.397$ s, when a relative maximum in the pressure coefficient field is detected at the left vertex of the body, which impacts the water pool. On the other hand, the descent of the medium weight wedge is more rapid and determines higher pressure levels in the fluid domain than the light wedge. As it penetrates faster into the water reservoir, the body reaches a symmetric and stable orientation (with null angular acceleration) more rapidly (since around $t = 0.421$ s), whilst the light wedge is still rotating.

Fig. 3.11 reports some examples of the field of the normalized velocity, where we can better appreciate the faster descent of the medium wedge, and a more accentuated deflection of its lateral jets with respect to the light wedge. No penetration of fluid particle into the solid domain (coloured in semitransparent black) occurs.

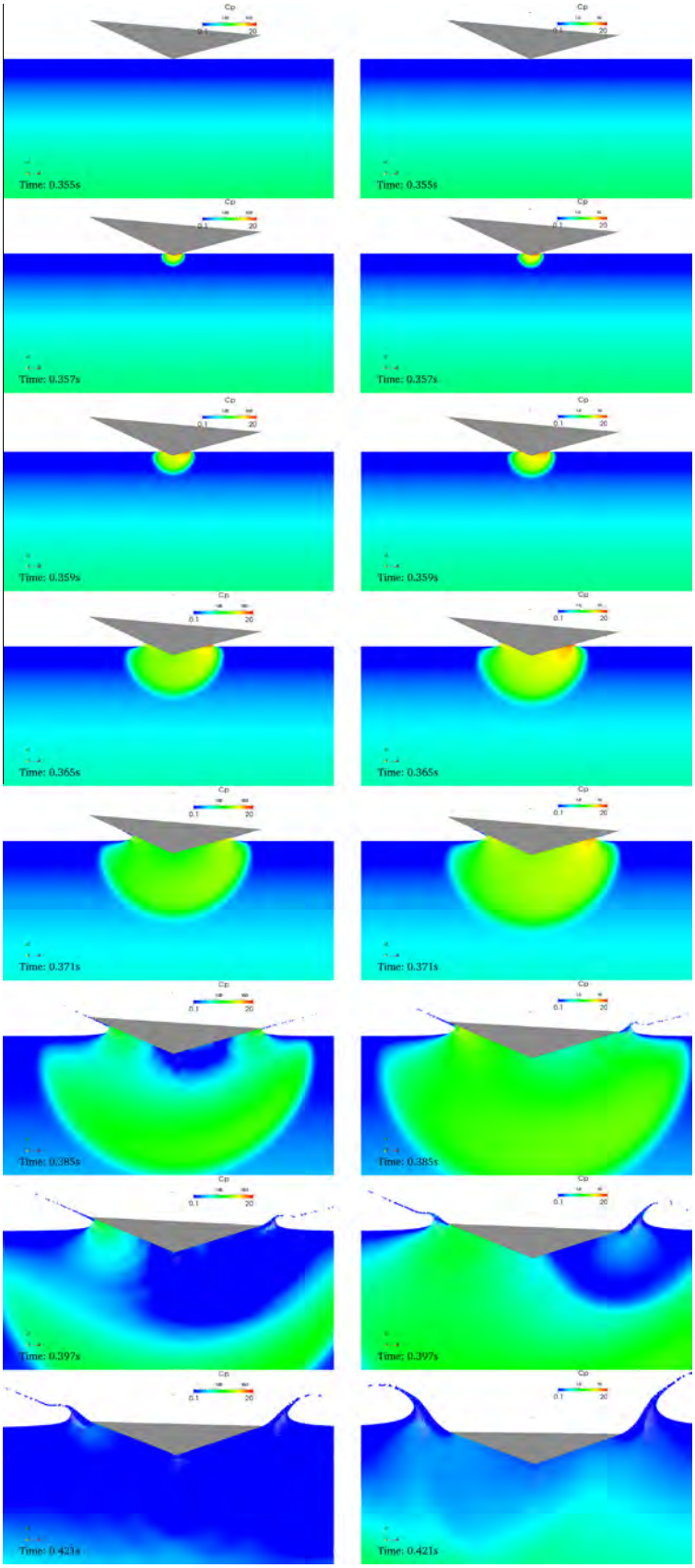

Fig. 3.10. Asymmetric water entries of solid wedges: time evolution of the field of the pressure coefficient. Left column: light wedge. Right column: medium wedge.

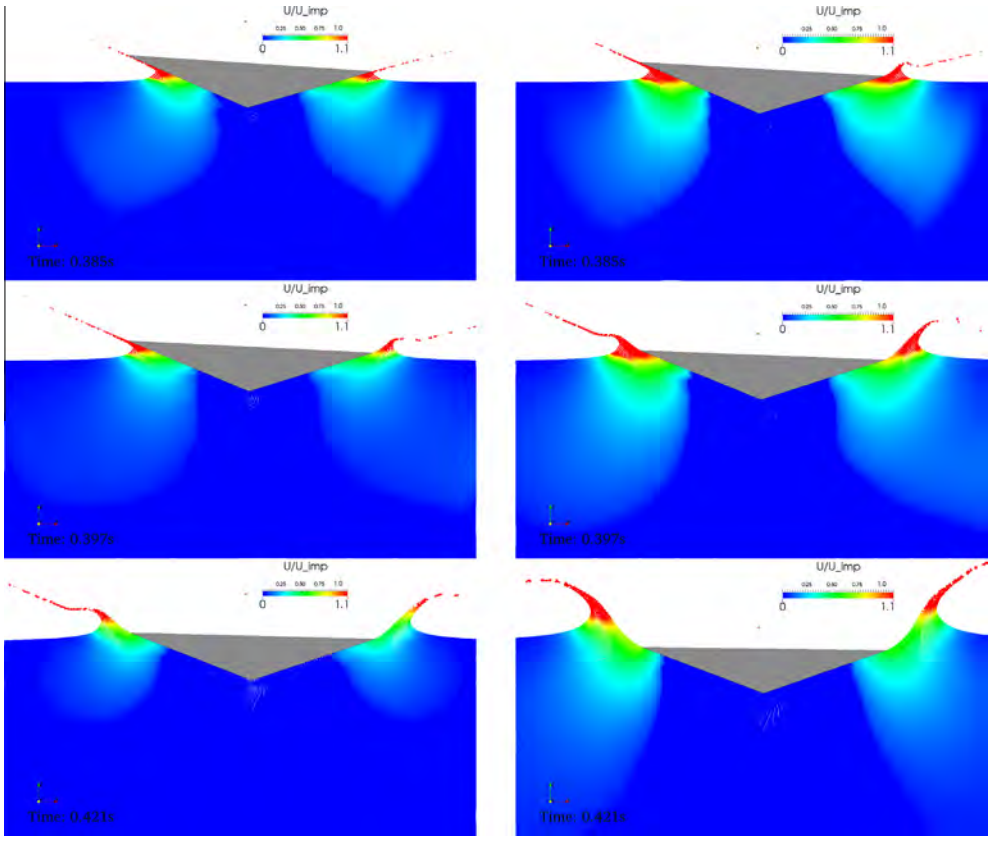

Fig. 3.11. Asymmetric water entries of solid wedges: time evolution of the field of the absolute value of the normalized velocity. Left column: light wedge. Right column: medium wedge.

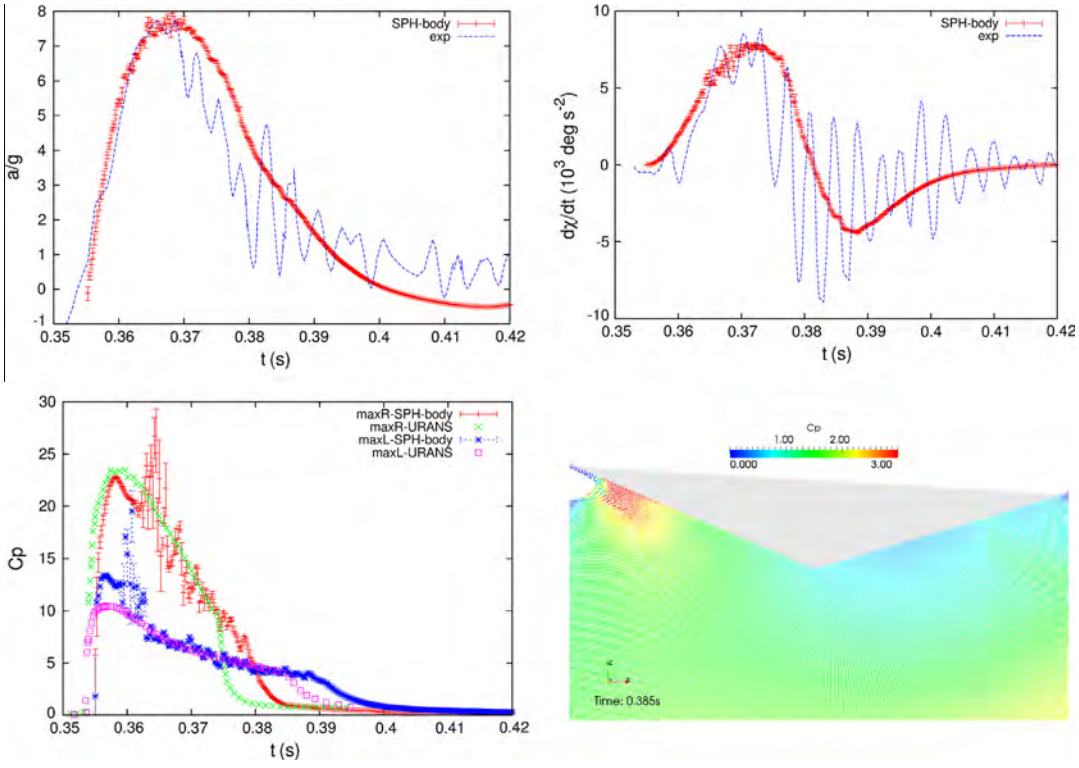

Fig. 3.12. Asymmetric water entry of a medium wedge. Top row. Left panel: time evolution of the normalized acceleration. Right panel: time evolution of the angular acceleration. Bottom row. Left panel: time evolution of the maximum value of the pressure coefficient over the wedge. Right panel: example of the field of the pressure coefficient. Validation and inter-comparisons.

3.4.4. Asymmetric water entry of a medium weight wedge (2D)

This section describes a quantitative validation concerning the asymmetric fall of a medium weight wedge (Table 3.1), while the pressure and velocity fields of this test case have already been analyzed in Section 3.4.3.

Fig. 3.12(top row) shows the comparisons between numerical and experimental values of the normalized acceleration (left panel) and angular acceleration (right panel). The first is well reproduced in terms of main time evolution and peak value. The angular acceleration is well represented as well, by correctly filtering the small scale oscillations (due to the deformability of the body, as already discussed).

The performance of the model is more reliable than the previous test case, as explained in the following. The main reason is related to the definition of the initial conditions, at the beginning of the water-body impact. Thanks to its higher mass and moment of inertia (2.4 and 1.2 time higher than those of Section 3.4.3, respectively), this heavier wedge is less sensitive to the aerodynamic forces and torques interesting the body before the impact. As a result, the agreement between experimental and SPH results is improved, especially in terms of angular acceleration (Fig. 3.12, top right panel).

In general, the maximum values (100th percentile) of pressure coefficient are satisfactorily reproduced (Fig. 3.12, bottom left panel), despite some local overestimations and a noisy time evolution on the right (R) side of the wedge. This is due to the relevant SPH truncation errors recorded between $t = 0.362$ s and $t = 0.367$ s, which affect the very 100th percentile of the C_p particle values during this limited period.

Finally, an example of the field of the pressure coefficient is shown in Fig. 3.12(bottom right panel). At this time, the vertex of the left side begins to impact the water pool. The spatial evolution of C_p is regular at boundaries and avoids penetrations of fluid particle into the solid body (coloured in semitransparency in Fig. 3.12).

3.5. Preliminary test: multiple interactions (3D)

The numerical model has been qualitatively tested over a simple 3D test case involving two bodies, which simultaneously interact with each other, several boundaries and a water front.

This test case is performed just to preliminary check the simultaneous behaviour of all the interaction terms introduced in Sections 2.3 and 2.4 and to further confirm that the fluid/body particles do not cross the body–body, fluid–body and body–boundary interfaces (to guarantee no mass penetration). Here we use

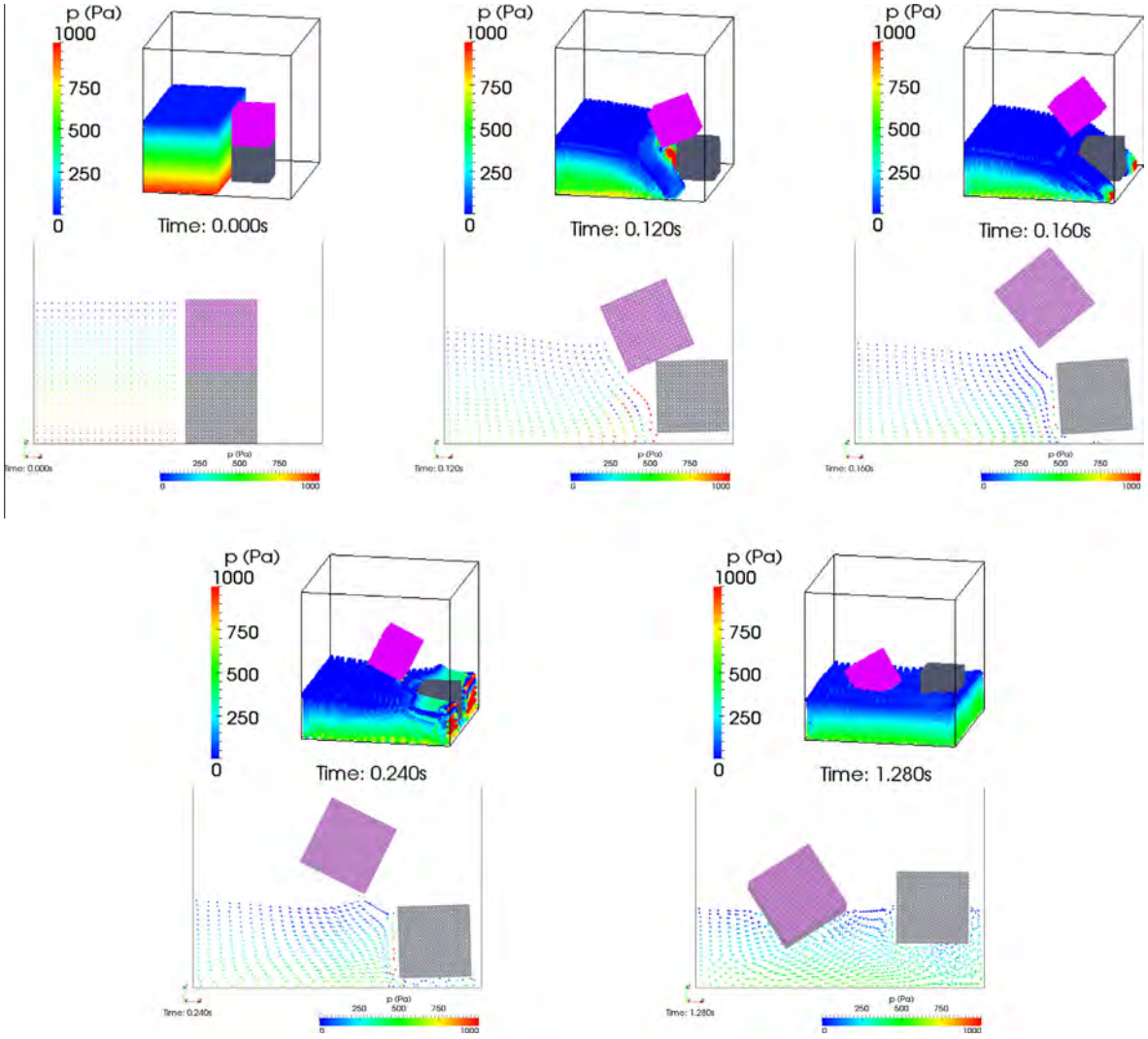

Fig. 3.13. Multiple interactions. Time evolution of the pressure field and the corresponding positions of the bodies. Superior rows: 3D view. Inferior rows: lateral view (only the few fluid particles at around $y = 0.100$ m are shown).

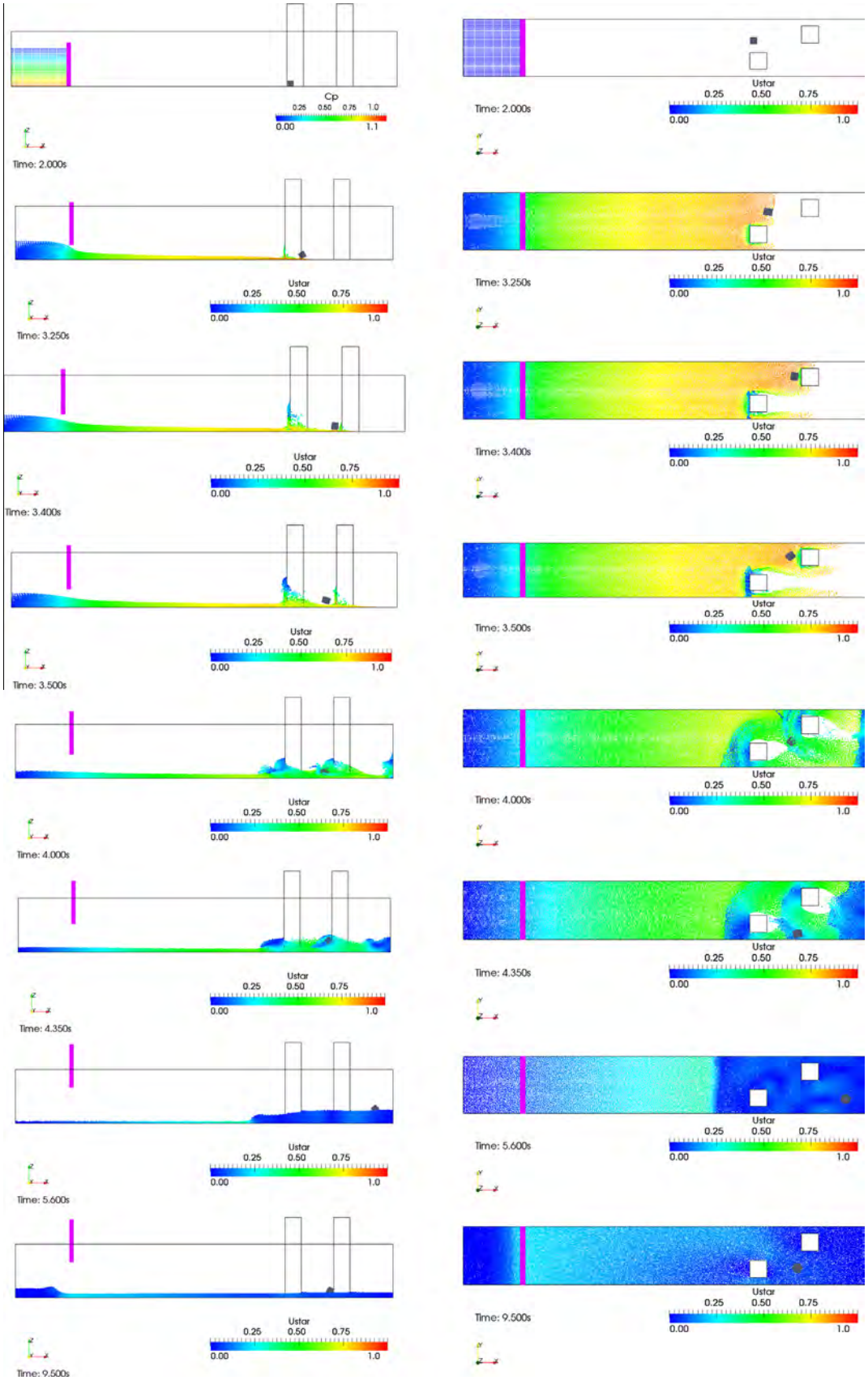

Fig. 3.14. Dam break with body transport. Time sequence of the field of the absolute value of the normalized velocity. Left column: lateral view. Right column: plan view.

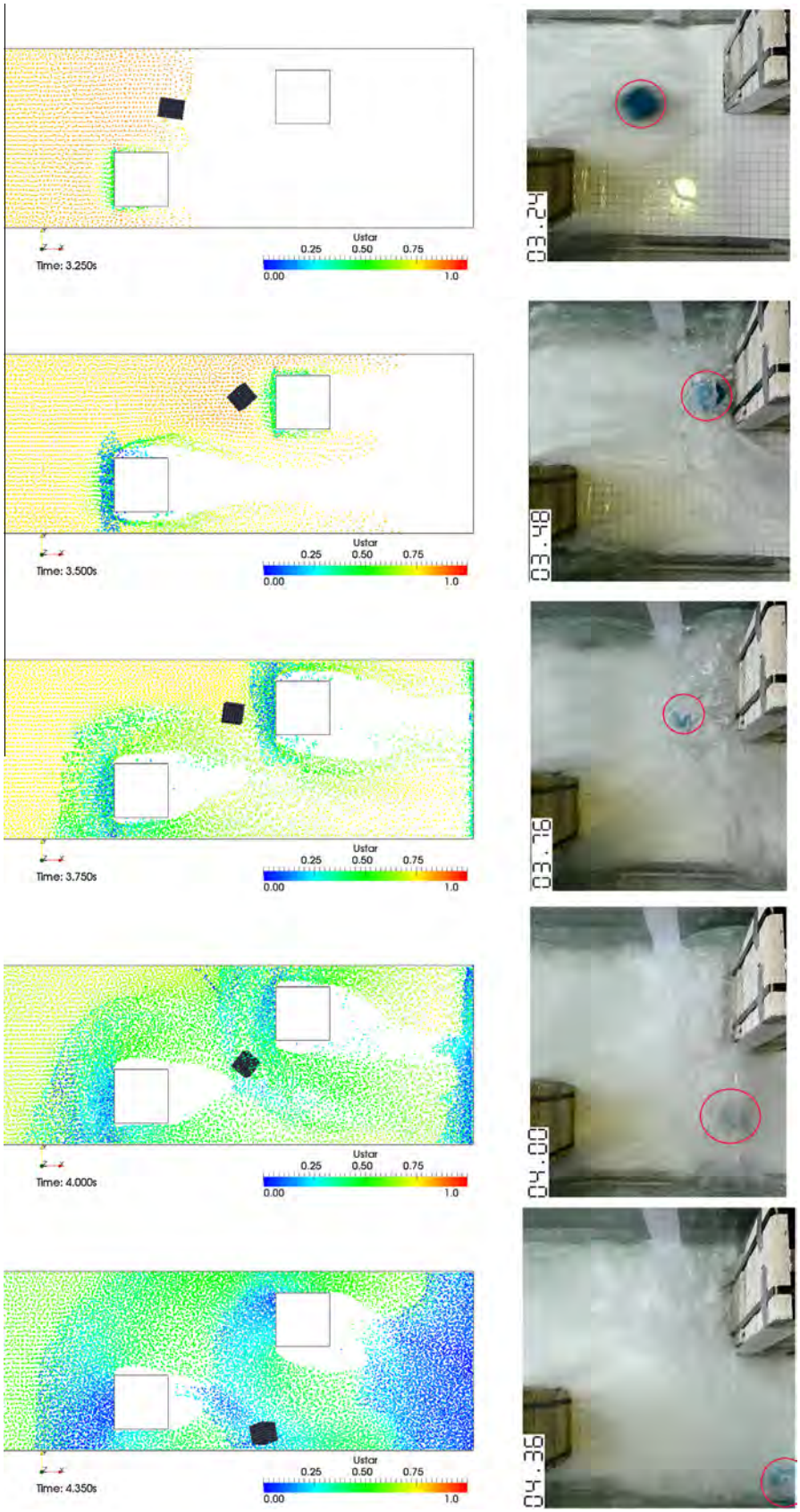

Fig. 3.15. Dam break with body transport. Graphical comparisons of the body trajectory. Left column: SPH model. Right column: experiment (red circles highlight the position of the body). (For interpretation of the references to colour in this figure legend, the reader is referred to the web version of this article.)

$dx = 0.005$ m, the tank is $0.200 \times 0.200 \times 0.100$ m^3, $dx/dx_s = 2.0$, $\rho_s/\rho = 0.5$. The bodies are cubes of length 0.050 m.

Fig. 3.13 shows the time evolution of the phenomenon (fluid particles are coloured according to the pressure levels). Initially, hydrostatic conditions are imposed. In the superior rows, we can appreciate the general features of the simulation (3D view). In the inferior rows, we just show the very few fluid particles which temporarily lie in a small slice at the centre of the domain (at y around 0.1 m). This allows checking the relative positions of fluid and body particles, which are instead all plotted. When the gate suddenly lifts, simulating a sort of dam break event, the water front impacts the inferior body ("body 1"), which impinges and pushes the superior solid ("body 2") upward and towards the water front ($t = 0.120$ s). At the same time, "body 1" remains confined by the lateral wall and begins to lift under the hydrodynamic pressure forces. "body 2" describes a parabolic trajectory in air ($t = 0.160$ s) and plunges into the water pool ($t = 0.240$ s). At later times ($t = 1.280$ s), the dynamics is slower and both the bodies begin to tend to an equilibrium position with their centre of mass closer to the free surface. The whole sequence shows that, still at the rough resolution here deliberately assumed, the non-permeability of solid bodies to fluid particles is guaranteed, as well as no body particle crosses any body–body or body–boundary interface. These are necessary conditions to be satisfied, before proceeding to further and more complex investigations (Sections 3.6 and 3.7). Finally, some apparently isolated particles are visible in this sequence, together with some pressure anomalies. They are related to the rough resolution here imposed (to eventually stress the model errors), and to the particular way we visualize fluid particles on the inferior rows of Fig. 3.13.

3.6. Dam break with body transport (3D)

The SPH model of Section 2 is here validated on a 3D experimental dam break event, which involves the transport of a floating body and the interactions with two fixed obstacles, a mobile gate (representing a dam) and fixed walls.

The experimental tests have been carried out during this study in the Hydraulics Laboratory of Basilicata University, on a tilting channel characterized by a rectangular cross section of 0.5 m in width and 0.6 m in height. The main structure of the channel is totally in steel, while the lateral walls are in transparent glass and the floor of the channel is in bakelite [56]. The flow inside the channel is derived by a water reservoir. An automatic mechanism opens the gate so quickly to obtain an event as possible similar to a dam-break.

The experiment provides some measurements of the body trajectory and free surface levels close to the two fixed obstacles, evaluated using an image analysis of Charge Coupled Device (CCD) cameras set on acquisition frequency of 24 fps, which allows a 3D validation of the model. Such cameras are located at different points of view thanks to a stainless steel modular system fixed to the channel structure. The experimental set-up represents the evolution of a dam break front as resulting from a regular (non-instantaneous) lifting of a gate, which initially confines the water reservoir. Further, this experimental configuration is more complex than others available in literature (e.g. [57,58]), because it represents the transport of a floating body and considers the presence of more than one fixed obstacle.

The gate begins to lift at $t = t_0 = 2.00$ s, with a uniform vertical velocity $w = 0.11$ m/s until $t = 5.00$ s, when it stops. The maximum value of the numerical acceleration was around 4–8 g, which still

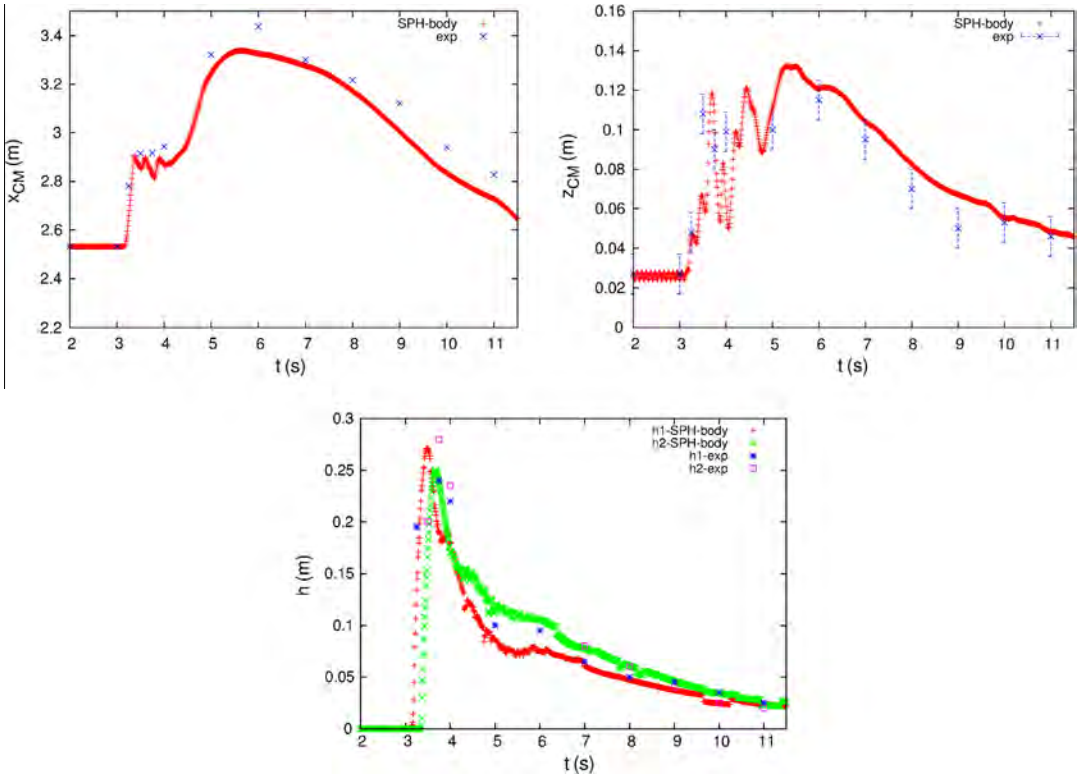

Fig. 3.16. Dam break with body transport: validations over experimental values. Top left: time evolution of the x-coordinate of the centre of mass of the body. Top right: time evolution of the height of the body barycentre. Bottom: time evolution of the free surface height (h) at the up-flow faces of obstacles 1 (up-flow) and 2 (down-flow).

remains under the threshold (10 g) we impose to avoid (2.21) providing an unreliable estimation of the body particle pressure. We set $dx/dx_s = 5/3$, with $dx = 0.0125$ m. The estimated parameters are normalized assuming the velocity scale $\sqrt{2gH} = 2.646$ s. The domain and the water reservoir dimensions are $3.500 \times 0.500 \times 0.500\ m^3$ and $0.500 \times 0.500 \times 0.350\ m^3$, respectively (Fig. 3.14, top left panel). The dimension of each obstacle is $0.150 \times 0.150 \times 0.750\ m^3$. The first one ("obstacle 1") is 2.5 m distant from the left boundary of the domain. The same distance measures 2.950 m for the down-flow obstacle ("obstacle 2"). Both are 0.060 m far from their closets vertical wall boundary. The transported body is a cube with side 0.054 m and mass $m_B = 0.073$ kg ($\rho_s = 464\ kg/m^3$). The body is initially at rest and its centre of mass is located 2.532 m far from the left boundary of the reservoir, 0.313 m from the right wall and 0.027 m from the bottom, where the body lies on. We prefer to optimize the initial position of the body by displacing of a very little quantity (smaller than the spatial resolution of the model) its initial y-coordinate, in order to provide the best initial conditions to the body dynamics, without deteriorating the model resolution. The gate is also modelled as a numerical body (not a frontier), but its kinematics is imposed. This means that its influence on the fluid domain fields is estimated according to the formulations described in Section 2.3. The gate size is $0.0376 \times 0.500 \times 0.400\ m^3$. Free surface is monitored on the up-wind faces of both the fixed obstacles.

Fig. 3.14 reports a time sequence of the field of the normalized velocity (left column: lateral view; right column: plan view). The water front impacts the upwind obstacle and moves upwards its upwind face. At the same time it transports the body down-flow, lifting it from the bottom ($t = 3.250$ s). The body then impacts the down-flow obstacle ($t = 3.40$ s) and bounces backward ($t = 3.50$ s) lifting up in air. It then falls down into water and is transported by the vortex in the recirculation zone of "obstacle 2". At around $t = 4.00$ s the body is deviated laterally, while the faster water front has reached the down-flow boundary of the domain and, simultaneously, two reflected surface waves move up-flow from each of the fixed obstacles they come from. At around $t = 4.0$ s, a first cavity zone is clearly detected in the wake of the "obstacle 1" (as also shown in Fig. 3.17). The wake of the down-flow obstacle develops later and interacts with the down-flow frontier of the domain. These cavity zones will be rapidly filled by both the water mass of the rest of the first water front and the surface wave, as it is reflected by the down-flow boundary ($t = 4.35$ s). The transported body now overpasses the upwind face of the downwind obstacle and remains in a stagnation zone close to the downwind frontier. At $t = 5.60$ s a single front wave moves towards the up-flow

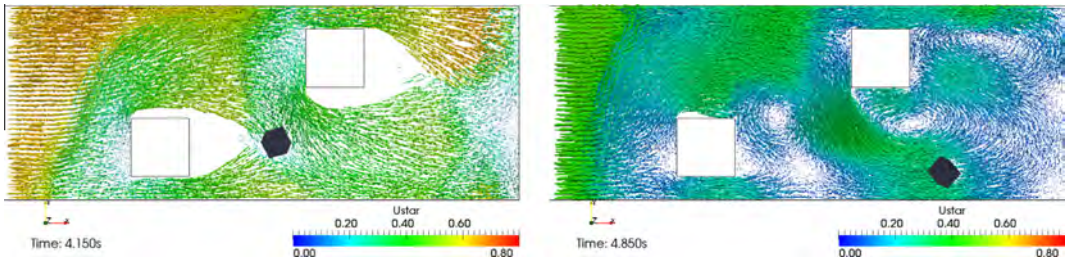

Fig. 3.17. Dam break with body transport. Fields of the vector of the normalized velocity.

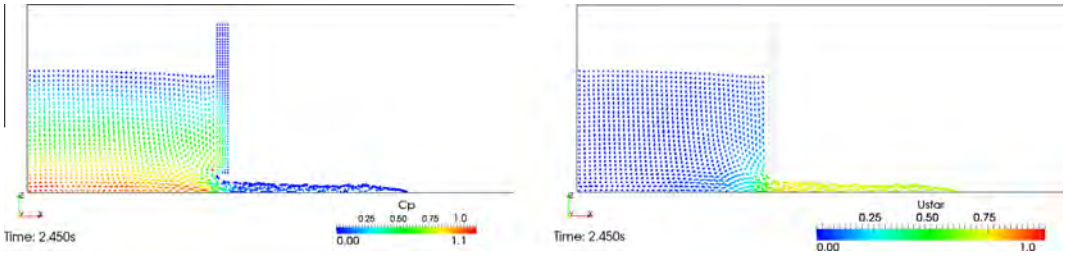

Fig. 3.18. Dam break with body transport: lateral view of the up-flow region of the domain. Left: field of the pressure coefficient (both fluid and body particles). Right: field of the absolute value of the normalized velocity (body particles are coloured in semitransparent black). (For interpretation of the references to colour in this figure legend, the reader is referred to the web version of this article.)

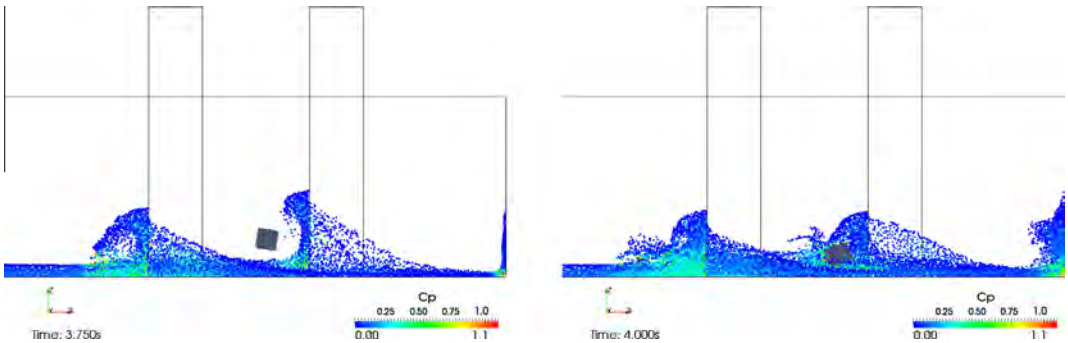

Fig. 3.19. Dam break with body transport. Details of the field of the pressure coefficient in the downwind region of the domain (lateral view).

frontier. The body is slowly transported by the flow far from the down-flow boundary, while the surface wave impacts the up-flow frontier and a second reflected wave is there generated, just few instants before $t = 9.5$ s.

Fig. 3.19 shows some examples of the fields of the pressure coefficient in the down-flow region of the domain (lateral view). The detailed images underline the main features of the breaking waves, occurring at 3.75 s and 4.00 s, after the water front is reflected by the fixed obstacles.

Fig. 3.15 provides a graphical comparison between the numerical and the experimental positions of the body. It approaches the obstacles ($t = 3.25$ s), impinges on it ($t = 3.50$ s), is transported within the recirculation region up-flow the obstacle ($t = 3.75$ s), deviates laterally ($t = 4.00$ s) and begins to overpass it ($t = 4.35$ s). The model can

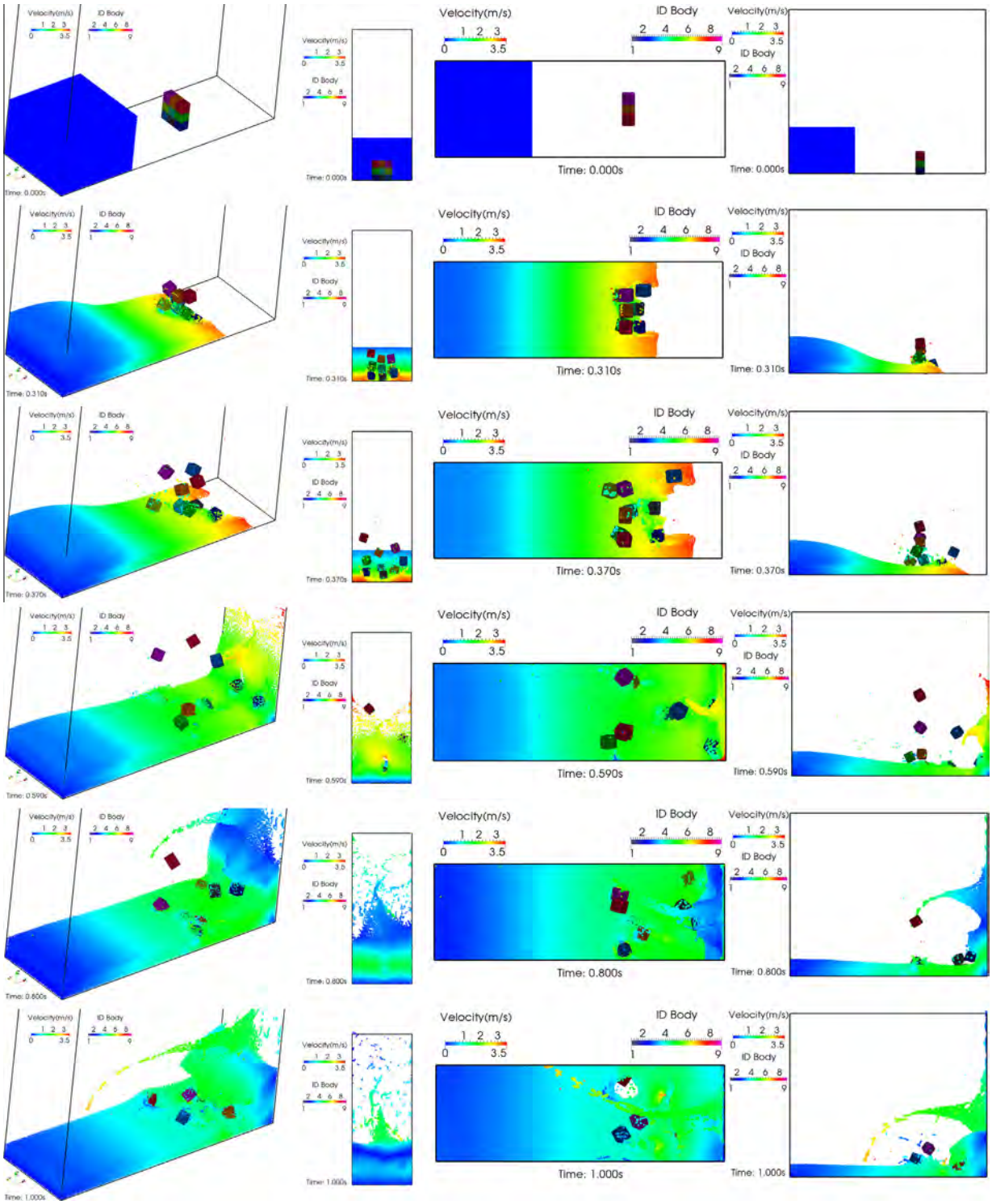

Fig. 3.20. Demonstrative test case. Dam break with simultaneous transport of 9 solid bodies. Sequence of snapshots with 3D, front, top and lateral view (from left to right), respectively. Fluid particles are coloured according to their absolute value of velocity; body particles refer to their body identification number. (For interpretation of the references to colour in this figure legend, the reader is referred to the web version of this article.)

correctly reproduce the body trajectory, even if the body dynamics is strongly non-linear in the recirculation zone of "obstacle 2".

Fig. 3.16 provides quantitative comparisons between the numerical results and the experimental data, in terms of body trajectory and free surface levels. Time evolution of the x-component of the centre of mass position is well reproduced by the model (Fig. 3.16, top left). The body begins to move at around 3.2 s and impacts the second obstacle. During the period $t = 3.4$–4.0 s the body is entrained in the recirculation region. It then deviates laterally and reaches a zone at low velocities, close to the down-flow frontier. At around $t = 5.5$ s it begins to move backward, transported by the main flow, while a reflected front wave move towards the gate. The model well reproduces the body trajectory along the x-axis. Nevertheless, some minor errors are still detectable, as the numerical body begins to move back a little earlier.

The experimental data concerning the vertical position of the body are reported in Fig. 3.16(top right panel). Their experimental errors are not negligible, as shown in the figure. Nevertheless, we can perform some quantitative comparisons and the numerical results well agree with the experimental data. The vertical position of the floating body is normally related to the position of the free surface at those horizontal coordinates. However, just after the first impact, the body moves in air (at around $t = 3.50$ s) after its impact against the down-flow obstacle. We notice that when the body moves backward the main flow around it is characterized by a decreasing free surface height, as water is filling the upper part of the domain, where the water levels are lower (Fig. 3.16).

The numerical estimations of the free surface levels on the up-flow faces of the obstacles are provided in Fig. 3.16(bottom panel). They are in good agreement with the experimental data, even if some underestimations are detected, especially for "obstacle 1".

Fig. 3.18 finally provides some details of the phenomenon in the region around the gate, while it is lifting up and still interacting with the water reservoir. We have an example of how the body particle pressure is reconstructed according to (2.21), and well matches the fluid field at the body surface (left image). On the right side of Fig. 3.18(field of the normalized velocity), we can appreciate that there is no penetration of fluid particles into the solid gate, whose body particles are coloured in semitransparent black (we would immediately appreciate any eventual fluid particle penetrating into the gate).

In this context, we notice that the transport of a solid body during a flood event is a highly non-linear phenomenon. In this frame, a statistical approach (based on the perturbations of the initial and/or boundary conditions) could provide more information and estimate the most probable body trajectories, simultaneously taking into account both the incertitude related to the boundary/initial conditions and the model accuracy, which is still dependent on the SPH spatial resolution due to the chaotic features of the phenomenon. Although a statistical approach is needed, this reference simulation still refers to the finest resolution available. The results are presented as expected values of the monitored parameters, whose probability density functions could be further quantified also in terms of statistical moments higher than the mean.

Finally, this test case provides a validation of the presented model in representing a controlled dam break event, with the 3D transport of a cubic floating body and multiple impacts against fixed obstacles and frontiers.

3.7. Demonstrative test case: multiple body transport (3D)

This test case considers a configuration analogous to Section 3.6, but dealing with 9 solid bodies and introducing the following minor modifications. The phenomenon lasts 1.00 s, the frontiers are 1.25 m high, the dam break is instantaneous (without mobile gate); the fixed obstacles are removed; the domain length is 1.5 m. 9 bodies together represent a sheet lying on the channel bottom, with $x_{CM} = 1.000$ m and $y_{CM} = 0.250$ m. The sheet is composed of 9 juxtaposed cubes of side 0.054 m. Each body mass is $m_B = 0.6$ kg, but the 9th body, which has a doubled mass. Fluid particles are discretized with $dx = 0.0075$ m.

Fig. 3.20 shows a sequence of snapshots of the phenomenon from several points of view. Fluid particles are coloured according to their absolute value of velocity, while body particles refer to the body identification number.

This complex 3D case is simply considered as a demonstrative test to preliminarily assess the model potentials in managing a relevant number of solid bodies, transported during a flood event.

4. Conclusions

This study has developed and validated a Smoothed Particle Hydrodynamics scheme for the 3D transport of rigid solids in free surface flows. It solves the balance equations for the 3D dynamics of rigid bodies, using the SPH formalism. The scheme is coupled to an existing Weakly Compressible (WC)-SPH basic model, which uses the "semi-analytic approach" for the fluid–boundary treatment [33]. This study has implemented fluid–body and solid–solid multiple coupling terms in the fluid dynamics SPH equations for both the main flow and the transported bodies. The fluid–body interactions are modelled according to the boundary treatment of Adami et al. [32], which validated it for 2D frontiers with an imposed kinematics. Here, this treatment is implemented and adapted to handle free-slip conditions and provide validations for 3D body transport in free surface flows. The solid–solid interactions (body–body and body–boundary impingements) are modelled according to the SPH boundary force particles of [1]. This formulation originally refers to impacts between single particles at high velocities. This study has implemented and extended this technique to deal with low velocity impingements of entire solid bodies.

The new numerical model is tested against a sequence of case studies, which are preliminary validations for fluid–body, body–body and body–boundary impacts (both at high and low velocities, or with multiple interactions), as well as a sequence of four water entries of falling solid wedges (2D). The numerical model is then validated on a complex 3D experimental test case, still realized during this study. This represents a 3D dam break event, which involves fixed obstacles, a mobile gate/dam and a transported floating body. Furthermore, we show the potentials of the model in a demonstrative test case: a dam break event with the transport of 9 solid bodies. We could then simultaneously test in 3D the fluid–solid and solid–solid interactions, whose modelling is peculiar of the numerical solution here presented. These validations, performed by comparisons with several experimental, theoretical and URANS and other SPH numerical results, show the reliability of the model in reproducing the 3D transport of rigid bodies, driven by free surface flows, such as floods or surface waves interacting with floating or mobile structures.

Acknowledgements

The work of the RSE authors has been financed by the Research Fund for the Italian Electrical System under the Contract Agreement between RSE SpA and the Italian Ministry of Economic Development – General Directorate for Nuclear Energy, Renewable Energy and Energy Efficiency, stipulated on July 29, 2009, in compliance with the Decree of November 11, 2012.

We acknowledge the CINECA award under the ISCRA initiative, for the availability of High Performance Computing resources and support. In fact, many HPC simulations related to this study refer to the following two HPC research projects: a) HSPHMI14 – High performance computing for Lagrangian numerical models to

simulate free surface and multi-phase flows (SPH) and the scalar transport in turbulent flows (MIcromixing); June 2014 – March 2015; Amicarelli A., G. Agate, G. Leuzzi, P. Monti, R. Guandalini, S. Sibilla; HPC Italian National Research Project (ISCRA-C2); competitive call for instrumental funds; b) HPCEFM15 – High Performance Computing for Environmental Fluid Mechanics 2015 (Italian National HPC Research Project); instrumental funding based on competitive calls (ISCRA-C project at CINECA, Italy); 2015 - in progress; Amicarelli A., A. Balzarini, S. Sibilla, G. Agate, G. Leuzzi, P. Monti, G. Pirovano, G.M. Riva, A. Toppetti, E. Persi, G. Petaccia.

References

[1] Monaghan JJ. Smoothed particle hydrodynamics. Rep Prog Phys 2005;68:1703–59.
[2] Liu MB, Liu GR. Smoothed particle hydrodynamics (SPH): an overview and recent developments. Arch Comput Methods Eng 2010;17:25–76.
[3] Vaughan GL. The SPH equations for fluids. Int J Numer Meth Eng 2009;79:1392–418.
[4] Vacondio R, Rogers BD, Stansby P, Mignosa P. SPH modeling of shallow flow with open boundaries for practical flood simulation. J Hydraul Eng 2012;138(6):530–41.
[5] Colagrossi A, Landrini M. Numerical simulation of interfacial flows by smoothed particle hydrodynamics. J Comput Phys 2003;191(2):448–75.
[6] Antuono M, Colagrossi A, Marrone S, Lugni C. Propagation of gravity waves through a SPH scheme with numerical diffusive terms. Comput Phys Commun 2011;182(4):866–77.
[7] Marrone S, Colagrossi A, Antuono M, Lugni C, Tulin MP. A 2D+t SPH model to study the breaking wave pattern generated by fast ships. J Fluids Struct 2011;27:1199–215.
[8] Marrone S, Bouscasse B, Colagrossi A, Antuono M. Study of ship wave breaking patterns using 3D parallel SPH simulations. Comput Fluids 2012;69:54–66.
[9] Patel MH, Vignjevic R, Campbell JC. An SPH technique for evaluating the behaviour of ships in extreme ocean waves. Int J Marit Eng 2009;151:39–47.
[10] Groenenboom PHL, Cartwright BK. Hydrodynamics and fluid–structure interaction by coupled SPH-FE method. J Hydraul Res 2010;48(Issue SUPPL.1):61–73.
[11] Antoci C, Gallati M, Sibilla S. Numerical simulation of fluid–structure interaction by SPH. Comput Struct 2007;85(11-14):879–90.
[12] Vacondio R, Rogers BD, Stansby PK, Mignosa P, Feldman J. Variable resolution for SPH: a dynamic particle coalescing and splitting scheme. Comput Methods Appl Mech Engrg 2013;256:132–48. http://dx.doi.org/10.1016/j.cma.2012.12.014.
[13] Delorme L, Colagrossi A, Souto-Iglesias A, Zamora-Rodriguez R, Botia-Vera E. A set of canonical problems in sloshing, Part I: Pressure field in forced roll – comparison between experimental results and SPH. Ocean Eng 2009;36:168–78.
[14] Shao JR, Li HQ, Liu GR, Liu MB. An improved SPH method for modeling liquid sloshing dynamics. Comput Struct 2012;100–101:18–26.
[15] Souto Iglesias A, Perez Rojas L, Rodriguez RZ. Simulation of anti-roll tanks and sloshing type problems with smoothed particle hydrodynamics. Ocean Eng 2004;31:1169–92.
[16] Pastor M, Haddad B, Sorbino G, Cuomo S, Drempetic V. A depth-integrated, coupled SPH model for flow-like landslides and related phenomena. Int J Numer Anal Meth Geomech 2009;33:143–72.
[17] Marongiu JC, Leboeuf F, Caro J, Parkinson E. Free surface flows simulations in Pelton turbines using an hybrid SPH-ALE method. J Hydraul Res 2010;47:40–9.
[18] Neuhauser M, Marongiu J-C, Leboeuf F. Coupling of the meshless SPH-ALE method with a finite volume method. In: Particle-based methods III: Fundamentals and applications – proceedings of the 3rd international conference on particle based methods, fundamentals and applications, Particles 2013: 2013. p. 939–48.
[19] Koukouvinis PK, Anagnostopoulos JS, Papantonis DE. An improved MUSCL treatment for the SPH-ALE method: comparison with the standard SPH method for the jet impingement case. Int J Numer Meth Fluids 2013;71(9):1152–77. http://dx.doi.org/10.1002/fld.3706.
[20] Maurel B, Potapov S, Fabis J, Combescure A. Full SPH fluid–shell interaction for leakage simulation in explicit dynamics. Int J Numer Meth Eng 2009;80(2):210–34.
[21] Grenier N, Antuono M, Colagrossi A, Le Touzé D, Alessandrini B. An Hamiltonian interface SPH formulation for multi-fluid and free surface flows. J Comput Phys 2009;228:8380–93.
[22] Price DJ. Smoothed particle hydrodynamics and magnetohydrodynamics. J Comp Phys 2012;231(3):759–94.
[23] Bate MR. Stellar, brown dwarf and multiple star properties from a radiation hydrodynamical simulation of star cluster formation. Mon Not R Astron Soc 2012;419(4):3115–46.
[24] Price DJ, Federrath C. A comparison between grid and particle methods on the statistics of driven, supersonic, isothermal turbulence. Mon Not R Astron Soc 2010;406(3):1659–74.
[25] Frenk CS, White SDM, Bode P, Bond JR, Bryan GL, Cen R, et al. The santa barbara cluster comparison project: a comparison of cosmological hydrodynamics solutions. Astrophys J 1999;525(2):554–82.
[26] Busini V, Marzo E, Callioni A, Rota R. Definition of a short-cut methodology for assessing earthquake-related Na-Tech risk. J Hazard Mater 2011;192(1):329–39. http://dx.doi.org/10.1016/j.jhazmat.2011.05.022.
[27] Liu MB, Liu GR, Lam KY. Constructing smoothing functions in smoothed particle hydrodynamics with applications. J Comput Appl Math 2003;155:263–84.
[28] Amicarelli A, Marongiu J-C, Leboeuf F, Leduc J, Caro J. SPH truncation error in estimating a 3D function. Comput Fluids 2011;44:279–96.
[29] Amicarelli A, Marongiu J-C, Leboeuf F, Leduc J, Neuhauser M, Fang Le, et al. SPH truncation error in estimating a 3D derivative. Int J Numer Meth Eng 2011;87(7):677–700.
[30] Monaghan JJ, Kajtar JB. SPH particle boundary forces for arbitrary boundaries. Comput Phys Commun 2009;180:1811–20.
[31] Basa M, Quinlan NJ, Lastiwka M. Robustness and accuracy of SPH formulations for viscous flow. Int J Numer Meth Fluids 2009;60(10):1127–48.
[32] Adami S, Hu XY, Adams NA. A generalized wall boundary condition for smoothed particle hydrodynamics. J Comput Phys 2012;231:7057–75.
[33] Di Monaco A, Manenti S, Gallati M, Sibilla S, Agate G, Guandalini R. SPH modeling of solid boundaries through a semi-analytic approach. Eng Appl Comput Fluid Mech 2011;5(1):1–15.
[34] Vila JP. On particle weighted methods and smooth particle hydrodynamics. Math Models Methods Appl Sci 1999;9(2):161–209.
[35] Ferrand M, Laurence DR, Rogers BD, Violeau D, Kassiotis C. Unified semi-analytical wall boundary conditions for inviscid laminar or turbulent flows in the meshless SPH method. Int J Numer Meth Fluids 2013;71(4):446–72.
[36] Mayrhofer A, Rogers BD, Violeau D, Ferrand M. Investigation of wall bounded flows using SPH and the unified semi-analytical wall boundary conditions. Comput Phys Commun 2013;184:2515–27.
[37] Ferrari A, Dumbser M, Toro EF, Armanini A. A new 3D parallel SPH scheme for free surface flows. Comput Fluids 2009;38:1203–17.
[38] Molteni D, Colagrossi A. A simple procedure to improve the pressure evaluation in hydrodynamic context using the SPH. Comput Phys Commun 2009;180:861–72.
[39] Amicarelli A, Agate G, Guandalini R. A 3D fully Lagrangian smoothed particle hydrodynamics model with both volume and surface discrete elements. Int J Numer Meth Eng 2013;95:419–50. http://dx.doi.org/10.1002/nme.4514.
[40] Oger G, Doring M, Alessandrini B, Ferrant P. Impulse-based rigid body interaction in SPH. J Comput Phys 2006;213:803–22.
[41] Monaghan JJ, Kos A, Issa N. Fluid motion generated by impact. J Waterw Port Coastal Ocean Eng 2003;129:250–9.
[42] Omidvar P, Stansby PK, Rogers BD. Wave body interaction in 2D using smoothed particle hydrodynamics (SPH) with variable particle mass. Int J Numer Meth Fluids 2012;68:686–705.
[43] Omidvar P, Stansby PK, Rogers BD. SPH for 3D floating bodies using variable mass particle distribution. Int J Numer Meth Fluids 2012;72(4):427–52. http://dx.doi.org/10.1002/fld.3749.
[44] Kajtar JB, Monaghan JJ. On the dynamics of swimming linked bodies. Eur J Mech B/Fluids 2010;29:377–86.
[45] Valizadeh A, Monaghan JJ. Smoothed particle hydrodynamics simulations of turbulence in fixed and rotating boxes in two dimensions with no-slip boundaries. Phys Fluids 2012;24(3) [Article no. 035107].
[46] Kajtar JB, Monaghan JJ. On the swimming of fish like bodies near free and fixed boundaries. Eur J Mech B/Fluids 2012;33:1–13.
[47] Hashemi MR, Fatehi R, Manzari MT. SPH simulation of interacting solid bodies suspended in a shear flow of an Oldroyd-B fluid. J Nonnewton Fluid Mech 2011;166:1239–52.
[48] Hashemi MR, Fatehi R, Manzari MT. A modified SPH method for simulating motion of rigid bodies in Newtonian fluid flows. Int J Non-Linear Mech 2012;47:626–38.
[49] Anghileri M, Castelletti LML, Francesconi E, Milanese A, Pittofrati M. Rigid body water impact – experimental tests and numerical simulations using the SPH method. Int J Impact Eng 2011;38:141–51.
[50] Seungtaik O, Younghee K, Byung-Seok R. Impulse-based boundary force (IBF). Comput Animat Virt Worlds 2009;20:215–24.
[51] Violeau D, Leroy A. On the maximum time step in weakly compressible SPH. J Comput Phys 2014;256:388–415.
[52] Areti K, Hendrickson K, Yue DKP. SPH for incompressible free-surface flows. Part II: Performance of a modified SPH method. Comput Fluids 2013;86(5):510–36. http://dx.doi.org/10.1016/j.compfluid.2013.07.016.
[53] Zoppé B. Simulation numérique et analyse de l'écoulement dans les augets des turbines Pelton. PhD thesis; Institut national polytechnique (Grenoble, France); 2004.
[54] Hay A, Leroyer A, Visonneau M. H-adaptive Navier–Stokes simulations of free-surface flows around moving bodies. J Mar Sci Technol 2006;11:1–18.
[55] Xu L, Troesch AW, Petterson R. Asymmetric hydrodynamic impact and dynamic response of vessels. In: Proceedings of 17th international conference on offshore mechanics and arctic engineering, 1998. p. 98–320.
[56] Mirauda D, Greco M, Volpe Plantamura A. Influence of the entropic parameter on the flow geometry and morphology. In: Proc. world academy of science, engineering and technology, ICWEE 2011, Phuket, Thailand; 2011. p. 1357–62.
[57] Gómez-Gesteira M, Dalrymple RA. Using a 3D SPH method for wave impact on a tall structure. J Waterw Port Coastal Ocean Eng 2004;130(2):63–9.
[58] Soares-Frazão SA, Zech Y. Experimental study of dam-break flow against an isolated obstacle. J Hydraul Res 2007;45(Supplement 1):27–36.